

RADU: Ray-Aligned Depth Update Convolutions for ToF Data Denoising

Michael Schelling
Ulm University

Pedro Hermosilla
Ulm University

Timo Ropinski
Ulm University

Abstract

Time-of-Flight (ToF) cameras are subject to high levels of noise and distortions due to Multi-Path-Interference (MPI). While recent research showed that 2D neural networks are able to outperform previous traditional State-of-the-Art (SOTA) methods on denoising ToF-Data, little research on learning-based approaches has been done to make direct use of the 3D information present in depth images. In this paper, we propose an iterative denoising approach operating in 3D space, that is designed to learn on 2.5D data by enabling 3D point convolutions to correct the points' positions along the view direction. As labeled real world data is scarce for this task, we further train our network with a self-training approach on unlabeled real world data to account for real world statistics. We demonstrate that our method is able to outperform SOTA methods on several datasets, including two real world datasets and a new large-scale synthetic data set introduced in this paper.

1. Introduction

Time of Flight (ToF) cameras are devices that are able to capture depth information of a scene by measuring the time the light emitted by the device needs to travel back once intersecting with an object. In practice, timing the reception of a light impulse requires precise and costly hardware and, as a result, consumer-level ToF cameras perform indirect measurements. The most common types are so-called Amplitude-Modulated Continuous-Wave (AMCW) ToF cameras, as they are for example used by the Kinect. The working principle of these AMCW cameras is to emit a periodically modulated light signal and retrieve the phase shift of the received signal, through which the travel time of the light and, consequently, the distance of the object to the camera is given [12]. However, the continuous illumination of the scene inevitably leads to Multi-Path Interference (MPI), as not only the direct reflection is received but also indirectly illumination which significantly impairs the depth estimation. Furthermore, these ToF cameras suffer

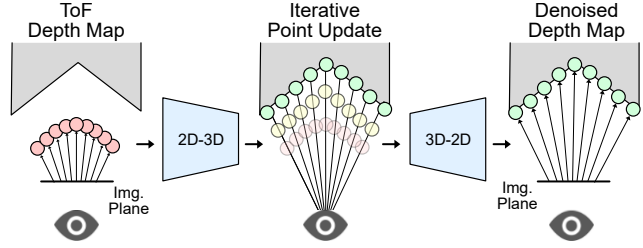


Figure 1. Given an initial ToF depth reconstruction our method projects the problem into a latent 3D space. The 3D point positions are updated iteratively along the camera rays using RADU point convolutions, in order to optimize the final 2D depth prediction.

from low Signal to Noise Ratios (SNR) on dark surfaces and the mixed pixel effect along sharp object edges [12].

Since deep learning approaches have shown great success in visual computing problems, many works have investigated the capabilities of 2D neural networks to denoise ToF depth images [1, 2, 4, 10, 11, 29]. However, existing methods treat the task of ToF denoising as a 2D image problem and do not take into account the explicit 3D information in their computations. In these works, the depth information is usually used as an input to standard Convolutional Neural Networks (CNN) for images [1, 2, 20, 27, 28], while the underlying 3D structure is not analyzed. In this work instead, we propose a new neural network architecture that projects the problem into the 3D domain and makes use of point convolutional neural networks [13] to analyze the noisy reconstruction and adjust the point positions along the view direction, see Fig. 1. This iterative process makes small changes to the point positions to reduce the noise level in between the convolutional layers and improve the final depth reconstruction. Further, we propose a novel fine-tuning procedure for Unsupervised Domain Adaptation (UDA) based on self-training methods, to transfer the knowledge acquired by our network from synthetic to real world ToF data. The effectiveness of this approach is evaluated on both synthetic and real world datasets and proves to be able to outperform existing methods. Moreover, we introduce a large-scale high-resolution dataset consisting of challenging scenes, containing high MPI levels, materials which pro-

duce low SNR captures and objects with high frequency details. In summary, our contributions are:

- A novel architecture for denoising of ToF images in a latent 3D space.
- A two-staged training procedure with a cyclic self-training approach designed to bridge the gap between synthetic and real world ToF images.
- A large-scale high-resolution synthetic ToF dataset containing measurements for scenes with high MPI.

Our synthetic data set, code and trained networks will be made publicly available in the future.

2. Related Work

In this section we will briefly review existing work related to our approach in different fields.

Learned ToF Denoising. Beginning with Marco *et al.* [20], several works on denoising ToF depth images using deep learning have been proposed. While the former uses an initial low-frequency ToF-depth prediction as input, subsequent work by Agresti *et al.* [1, 2] greatly improved the reconstruction by considering additional multi-frequency features derived from raw camera measurements to further reduce the noise. The same year, Su *et al.* [29] proposed a generative approach that generates depths directly from raw camera measurements. Instead of predicting a denoised depth directly, Guo *et al.* [10] followed an inverse approach and used a 2D CNN to denoise the raw camera measurements prior to the LF2 [33] depth reconstruction algorithm of the Kinect2. Further, several works on improving on various aspects and applications using machine learning followed, *e.g.* online calibration using RGB information [26], frame rate optimization [5], power efficiency [6], robotic arm setups [27] or translucent materials [28], to name a few. The aforementioned approaches all use standard 2D CNNs and thus consider the denoising problem as an image task.

Recent work aims to estimate the real depth by reconstructing the transient image, *i.e.* the impulse response of the scene, through learning methods. Burrato *et al.* [4] used the assumption that the direct reflection reaches the camera sensor early and predict the intensity and arrival time of the first two peaks of the impulse response. The iToF2dToF method [11] first predicts ToF depths at various frequencies which are used to estimate the two leading coefficients of the Fourier-Transform of the impulse response. While transient reconstruction is a promising direction, these methods are, as of now, still very memory demanding, and can thus only query few pixels in parallel, and do not reach the denoising capabilities of learned denoising approaches.

In contrast to previous work on ToF-denoising, we propose to lift the problem into 3D and use 3D point CNNs. With this approach we follow the findings of recent research, that neural networks can benefit from latent 3D rep-

resentations in various tasks, such as object detection [31] using 3D voxel CNNs on lidar data, semantic segmentation [35] using 2.5D convolutions on RGB-D data or even image generation [23].

Domain Adaptation for ToF Images. Real ToF data with labeled ground truth data is only sparsely available, as its collection is rather complex. Thus various synthetic data sets have been introduced [2, 10, 20] to provide the amount of data needed to train deep neural networks. However the usage of data from a different source, in this case a synthetic simulation, comes at the cost of introducing a domain gap, *i.e.* real and synthetic images differ in their statistical properties. Consequently, one major challenge when learning the task of denoising ToF images is bridging the domain gap between synthetic data sets and real world data.

To improve performance on real data Marco *et al.* [20] pre-train an auto-encoder network on unlabeled real world ToF-data, and transfer the encoder layers to a encoder-decoder network for denoising. Other works [1, 29] have suggested to use adversarial losses, where a second network acts as an adversarial agent which is trained to distinguish depths generated from real and synthetic data. During training the generator is optimized to deceive the discriminator.

Recently, self-training methods, which originated from a student-teacher approach by Hinton *et al.* [14], have shown great success in various variants of domain-adaptation [17–19, 21, 25, 34, 37, 38]. Building upon these works, we employ a cyclic self-training procedure to adapt our network to real world statistics by generating pseudo-labels for unlabeled real data, after pre-training the network on synthetic data.

3. Problem Statement

To estimate the distance d of an object, an AMCW ToF camera emits a light signal s_e , which is typically modulated by a sinusoidal periodic function, in the form of

$$s_e(t) = s_0 \cdot (1 + m \cdot \sin(2\pi ft)), \quad (1)$$

where s_0 is the average intensity, m is the modulation coefficient, f is the modulation frequency, and t is the time. For compactness and *w.l.o.g.* we neglect s_0 and m in the following and assume them to be equal to one. In the optimal case of only direct reflection the received light s_r is a scaled and phase shifted version of the emitted signal

$$s_r(t) = r \cdot s_e(t - \Delta t) = r \cdot (1 + \sin(2\pi ft - \Delta\varphi)), \quad (2)$$

where r is the ratio of the light backscattered to the sensor from the surface, and $\Delta\varphi$ is the phase delay after the signal has traveled the distance $2d$, *i.e.* $\Delta\varphi = 2dc/f$, where c is the speed of light. The received signal is averaged during the exposure time δt at the sensor with a phase shifted

version of the emitted signal, resulting in the measurement

$$m_\theta = \frac{1}{\delta t} \int_{\delta t} s_r(t) \cdot s_e \left(t + \frac{\theta}{2\pi f} \right) dt. \quad (3)$$

Under the assumption $\delta t \gg 1/f$ the measurement m_θ can be approximated as [7]

$$m_\theta = I + A \cdot \cos(\Delta\varphi + \theta), \quad (4)$$

where I is called the intensity and A the amplitude. By measuring m_θ for multiple phase offsets θ the phase shift $\Delta\varphi$ and the distance d can be reconstructed as [12]

$$\Delta\varphi = \arctan \left(\frac{\sum_\theta -\sin(\theta) \cdot m_\theta}{\sum_\theta \cos(\theta) \cdot m_\theta} \right), \quad (5)$$

$$d = \frac{c \cdot \Delta\varphi}{4\pi f}. \quad (6)$$

Due to the periodic nature of the signal, the reconstructed distance d using Eq. (6) is ambiguous for distances larger than $d_{max} = c/(2f)$. To resolve this so called phase-wrapping the common solution is to acquire measurements for different modulation frequencies f_k , which thus also have different maximal distances d_{max} .

In practice the received signal s_r is not only the direct reflection after the time Δt , as in Eq. (2), but a composition of light scattered along various paths P in the scene

$$s_r(t) = \int_P r(p) \cdot (1 + \sin(2\pi f t - \Delta\varphi(p))) dp. \quad (7)$$

While the intensity $r(p)$ can be expected to be low after multiple reflections on an isolated path p , the accumulation over all possible paths P leads to the aforementioned notable MPI distortion in the distance recovery, Eq. (6). Additionally, ToF-sensors suffer from the common camera noise sources in the form of photon shot noise, thermal shot noise and read noise, which are typically modeled jointly as an additive Gaussian noise on the measurement m_θ .

Although, d from Eq. (6) denotes the distance, it is commonly referred to as ToF depth, as we will do in this work.

4. Proposed Method

In this work we propose to incorporate 3D learning techniques to exploit the spatial structure of the scene geometry. In contrast to 2D convolutions, where spatial relations are encoded implicitly in the pixel grid location, a 3D convolution relies on explicitly given 3D coordinates [13]. In order to represent the 2.5D data in 3D space we use the inverse of the camera projection $\mathcal{P}_{G \rightarrow C}$ to create an initial spatial position for each pixel, as illustrated in Fig. 2. This allows us to denoise the depth in global coordinates, allowing the 3D layers to consider the 3D neighborhoods of the individual

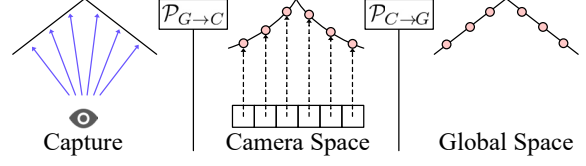


Figure 2. The non-parallelism of camera rays (left) leads to a distortion in the resulting depth image, as the camera measures the distance along the rays (middle). By applying the inverse camera projection $\mathcal{P}_{C \rightarrow G}$ the depth map is projected into 3D space, and, in the ideal case, aligns with the scene geometry (right).

pixels, and learn on the actual scene geometry, undistorted by the non-linear camera transformation.

In the case of ToF-data we derive an initial 3D coordinate from the ToF depth given by Eq. (6). Of course this initial depth is inherently noisy, and we assume that a 3D network would benefit from denoised 3D positions, which lie closer to the scene geometry. Thus, we propose to iteratively update the 3D positions of the points, enabling the network to optimize the latent point cloud in between the networks 3D layers. To keep the point position in alignment with the underlying structure given by the pixel position, we restrict the points movement to the respective camera ray.

However, compared to 2D Convolutions, 3D Convolutions are more demanding in compute power and memory consumption. To reduce this load we embed our proposed 3D layers in a 2D Network and introduce 2.5D pooling layers to reduce the spatial resolution in the 3D convolutions. This is necessary as for example a 320×240 image would result in 76.8k points, for comparison common networks for 3D object recognition typically use 1k points per model.

In the following we will first define the 2.5D pooling and the RADU convolution layers, before describing our network architecture, the loss function and the self-cycled training procedure for domain adaptation.

4.1. 2.5D Pooling

Several methods have been proposed for pooling operations on 3D point clouds, *e.g.* Poisson disk sampling [13] and cell average sampling [30]. However these methods suffer from drawbacks when applied to 2.5D data. Cell average sampling creates a new point as the mean point in a pre-defined 3D grid, which in general does not lie on the camera ray of a pixel. Poisson disk sampling chooses a subset of the given points based on their distances in 3D space, making these points still align with the original camera-rays. However this method aims to optimize the distribution of points in 3D space, which can result in non-uniform distributions when projected back into 2D space.

Instead, we propose a 2.5D pooling operation which pools the points in 3D according to their structure induced by the pixel grid, by considering the points' 2D neighbor-

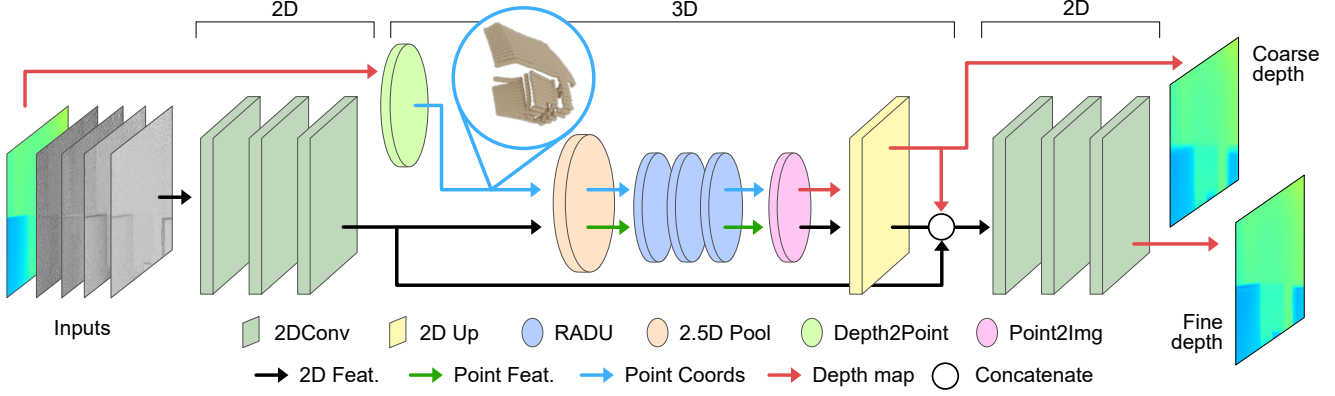


Figure 3. Proposed network architecture. We embed the 3D RADU convolutions in two 2D blocks and use an initial ToF depth given by Eq. (6) to compute initial spatial positions for the 2D features. After the 3D block the point coordinates updated by the RADU layers are projected back to a coarse depth image, which is used as an additional input feature to the following 2D block.

hoods given implicitly through the pixel grid and the camera ray direction associated with the corresponding pixel. For this we pool only the depth value of the 3D points of a $k \times k$ 2D patch using an order invariant operation, *e.g.* maximum or average pooling, and place a point with the pooled depth on the respective camera ray at the desired reduced resolution $N/k \times N/k$. The feature of the resulting point is computed by performing a second pooling operation on the features inside the points 2D neighborhood.

This way each resulting point represent a 2D neighborhood of fixed size and aligns with the camera rays. Note that this is different from (a) pooling the three point coordinates directly, where the result is not necessarily aligned with the camera rays, and (b) 2D pooling on the distance image, as the projections $\mathcal{P}_{G \rightarrow C}$ and $\mathcal{P}_{C \rightarrow G}$ are non-linear, see Fig. 2. Furthermore, this allows us to exploit existing 2D Pooling operations, dropping the need for costly 3D neighborhood and sampling computations for pooling.

4.2. Ray Aligned Depth-Update

In order to optimize the point position during the network execution, we propose to extend a given 3D convolu-

tion to predict an additional feature channel per layer. This value is used to shift the point along the respective camera ray, which we call Ray Aligned Depth Update (RADU) convolution. By updating along the camera ray, the point position stays consistent to the 2.5D nature of the point cloud, see Fig. 1. In order to stabilize the depth updates we regularize the update p^u to the range $(-\alpha, \alpha)$ using a scaled tanh function. In our experiments we set $\alpha = 0.1$, and provide an ablation study on different values for this hyperparameter in the supplementary. Formally, given a 3D convolution operator conv , a point cloud $\{p_i^{in}\} \subset \mathbb{R}^3$ with associated camera rays $\{r_i\} \subset \mathbb{R}^3$, and input features $\{f_i^{in}\} \subset \mathbb{R}^{C_{in}}$, the RADU convolution on point p_j^{in} with neighborhood $\mathcal{N}_j \subset \mathbb{N}$ is given as

$$(f_j^{out}, p_j^u) = \text{conv}(\{f_i^{in}\}_{i \in \mathcal{N}_j}, \{p_i^{in}\}_{i \in \mathcal{N}_j}), \quad (8)$$

$$p_j^{out} = p_j^{in} + \alpha \cdot \tanh(p_j^u) \cdot r_j, \quad (9)$$

where f_j^{out} is the output feature of the point p_j^{out} .

This extension is independent of the type of 3D-convolution used, in our experiments we implement it based on the Monte-Carlo-Convolution [13], which is illustrated in Fig. 4. This type of 3D-convolution has been shown to work well with non-uniformly sampled point clouds, as in our case where the density varies with the distance of the points to the camera, which we also investigate in Sec. 6.4.

4.3. Network Architecture

Our network architecture is illustrated in Fig. 3. It consists of an initial stack of three 2D convolutions with kernel size 3×3 , which is followed by a 2.5D pooling layer, using average pooling on both depth and features, with a stride of 8×8 . This 2D block is followed by a stack of three 3D RADU convolutions with increasing receptive fields of $0.1m$, $0.2m$, and $0.4m$. After the 3D block we use bi-linear upsampling to increase the spatial resolution of the

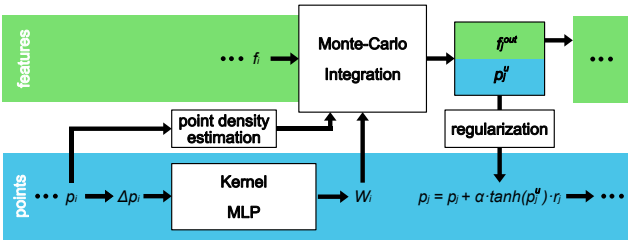


Figure 4. Realization of our RADU convolutional layer based on a 3D Monte-Carlo Convolution. In contrast to standard 3D point convolutions the spatial positions are not only used to predict the kernel weights but are also updated after each convolution.

intermediate features and the updated depth values. The coarse depth prediction of the 3D block is projected back into 2D using the inverse camera transform. Both the up-scaled depth and features are processed by a second block of three 2D convolutions with kernel size 3×3 . We further introduce a skip connection between the 2D blocks. In between convolutions we use leaky ReLU as a non-linearity.

As input to our method we use the same multi-frequency ToF features used in the works of Agresti *et al.* [1, 2]. That is, given measurements at three different frequencies f_k , $k = 1, 2, 3$, we use five input features, $d_1, d_2 - d_1, d_3 - d_1, A_2/A_1 - 1$, and $A_3/A_1 - 1$, where d_k is the ToF depth and A_k is the amplitude at frequency f_k . We follow the argumentation of Agresti *et al.* [2], that the differences $d_1 - d_k$, $k = 2, 3$ encode the frequency dependent influence of MPI on the depth recovery, and the relative amplitudes A_1/A_k , $k = 2, 3$ provide information about the strength of the MPI for a given pixel. The depth d_1 further serves as initial ToF depth for the projection $\mathcal{P}_{C \rightarrow G}$ into 3D space. Further, we augment the input data using rotation, mirroring and noise, a more detailed description of the data augmentation can be found in the supplementary material.

4.4. Coarse-Fine Loss

The 3D block of our network architecture produces an intermediate coarse depth estimate which is fed as an additional input to the subsequent 2D layers. To guide the network to predict an adequate representation of the 3D geometry we optimize both the final output \hat{d}_{out} and the coarse 3D representation of the 3D blocks \hat{d}_{3D} :

$$\mathcal{L} = \|d_{gt} - \hat{d}_{out}\|_1 + \|d_{gt} - \hat{d}_{3D}\|_1. \quad (10)$$

As the coarse depth \hat{d}_{3D} is not predicted by the final layer of the 3D network but is constructed iteratively as

$$(\hat{d}_{3D})_j = \mathcal{P}_{G \rightarrow C} \left(d_j^{init} + \sum_{l=1}^3 \alpha \cdot \tanh(p_{j,l}^u) \cdot r_j \right), \quad (11)$$

this allows each RADU layer to receive gradients directly from the loss function, preventing vanishing gradients, which is comparable to the influence on gradient flow of skip connections. However, as each layer is optimized to produce correctly denoised depths, this also increases the risk of overfitting. The influence of the choice of α is further discussed in the supplementary.

4.5. Unsupervised Domain Adaptation

To improve the performance of our method on real data we investigate a cyclic self-training procedure, derived from existing self-training methods for other tasks [17–19]. We evaluate a network, which is pre-trained on synthetic data, on unlabeled real data and use the predictions as pseudo labels in the following training phase. During training we

Algorithm 1 Adapted Cycled Self-Training Procedure

Require: $n_{cycle} \in \mathbb{N}, p \in [0, 1], D_{real}, D_{syn}$, network N

for $epoch$ **do**

if $epoch \bmod n_{cycle} \equiv 0$ **then**

$F_{in} \leftarrow D_{real}$ ▷ Get real world data

$\hat{d}_{out} = N(F_{in})$ ▷ predict, unaugmented

$S_2 \leftarrow \{d_{gt} : \hat{d}_{out}\}$ ▷ Save pseudo labels

end if

for *training step* **do**

if $rand.unif([0, 1]) < p$ **then**

$(F_{in}, d_{gt}) \leftarrow D_{real}$ ▷ Real with pseudo label

else

$(F_{in}, d_{gt}) \leftarrow D_{syn}$ ▷ Synthetic with label

end if

$(F_{in}, d_{gt}) = augment(F_{in}, d_{gt})$

$(\hat{d}_{out}, \hat{d}_{3D}) = N(F_{in})$

$minimize \mathcal{L}$, Eq.(10), on $(\hat{d}_{out}, \hat{d}_{3D})$

end for

end for

choose randomly between synthetic data with labels and real data with pseudo-labels, to prevent the network from overfitting to the pseudo-labels. We repeat this process multiple times by updating the pseudo-labels every n_{cycle} epochs. To avoid providing the exact same input during pseudo label generation and training we create pseudo-labels on unaugmented data and use augmented input during training. The procedure is summarized in Algorithm 1.

We refrain from training a teacher network on labeled real world data for pseudo-label generation to keep the assumption of U-DA and to make our approach applicable to settings where no labeled real data is available.

5. Cornell Box ToF Dataset

To allow a more broad evaluation of our method, we generate a new large scale synthetic dataset. As recent advances

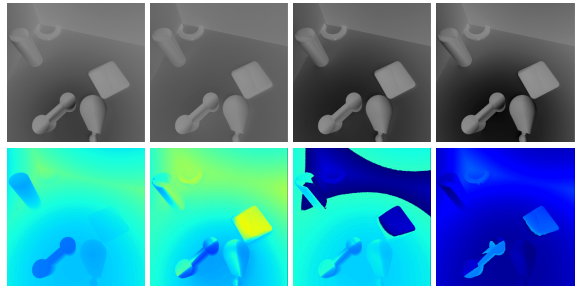


Figure 5. Example scene from our Cornell-Box dataset. The top row shows the four measurements m_θ at 20MHz, bottom row shows, from left to right, ground truth depth and ToF depths using Eq. (6) at 20MHz, 50MHz, and 70MHz, with phase wrapping.

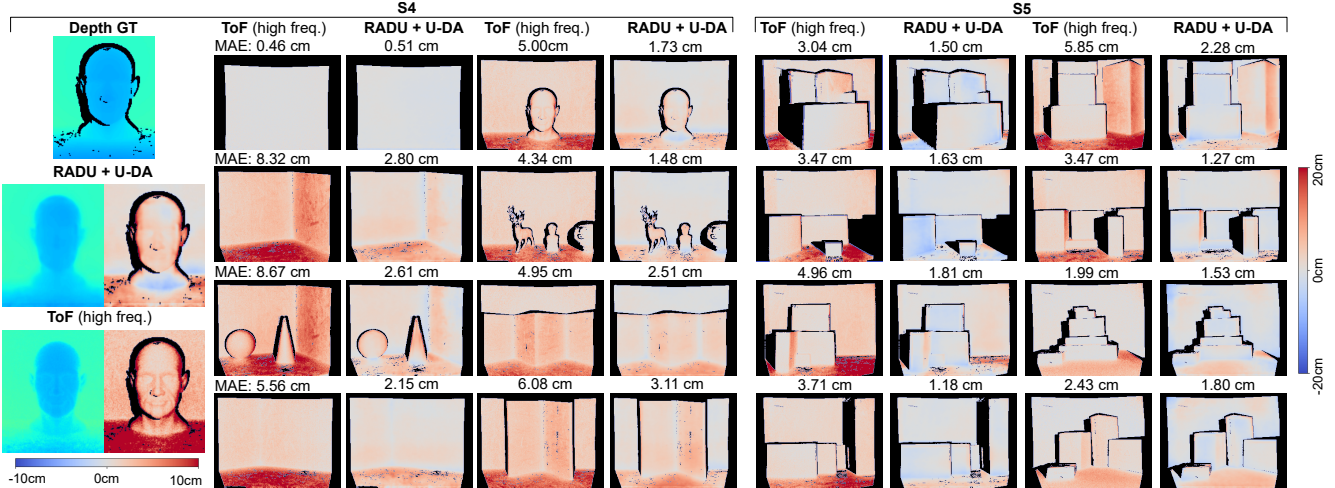


Figure 6. Depth error maps with MAE on the real datasets S4 (left) and S5 (right) of our method using both RADU convolutions and cyclic self-training for unsupervised domain adaptation. Areas where no ground truth depth is available are masked in black. The zoom in on the left displays both depth and error, with enhanced color coding on the error.

in ToF-camera hardware [22] could allow for higher resolution ToF sensors in the future, we render our dataset at a comparably high resolution of 600×600 pixels. Inspired by Miller *et al.* [22] we simulate the properties of a Raspberry Pi 3 camera equipped with an EAM for modulation.

To create a challenging setup for ToF-denoising we generate 142 scenes inspired by the Cornell box layout [9], to ensure high levels of MPI. We render each scene from 50 viewpoints with 3 different material properties, including dark materials for low SNR values, which results in 21.3k different renderings. The data is split into 116 training scenes, 13 validation scenes, and 13 test scenes. Each rendering is processed to simulate raw measurements for sinusoidal modulations at 20MHz, 50MHz, and 70MHz at phase offsets at $0, \pi/2, \pi$, and $3\pi/2$, resulting in 12 correlation measurements per capture. To our knowledge our dataset exceeds existing ToF datasets in both size and resolution, see Table 1. We refer the reader to the supplementary for further details about the dataset.

| Dataset | Type | GT | m_θ | Size | Resolution |
|-------------|------|-----|------------|-------|------------------|
| S1 [2] | Syn. | Yes | No | 54 | 320×240 |
| S2 [1] | Real | No | No | 96 | 320×239 |
| S3 [1] | Real | Yes | No | 8 | 320×239 |
| S4 [1] | Real | Yes | No | 8 | 320×239 |
| S5 [2] | Real | Yes | No | 8 | 320×239 |
| FLAT [10] | Syn. | Yes | Yes | 1.2k | 424×512 |
| Cornell-Box | Syn. | Yes | Yes | 21.3k | 600×600 |

Table 1. Properties of the datasets considered in our experiments.

6. Experiments

First we test our method on the established data sets of Agresti *et al.* [1,2], who provide a synthetic and several real data sets for the SoftKinect camera, containing both MPI and shot noise, to evaluate our method including U-DA. We refer to these data sets using the same notation as previous authors [1,4], see Tab. 1. As the real world datasets are rather small, we further evaluate our method on larger synthetic datasets, our dataset described in Sec. 5, where we additionally consider phase wrapping in the input features, and the FLAT dataset [10], which simulates a Kinect2 sensor, to also investigate the influence of non-sinusoidal modulations of $s_e(t)$, which violate the assumptions from Sec. 3.

Further we perform an ablation experiment, comparing RADU layers to other convolution layers. For additional informations about hyperparameter settings and other aspects of the experiments we refer to the supplementary material.

6.1. Experiment 1: Real World Data

The dataset S1-S5 contain intensities, amplitudes and phase unwrapped ToF depths. Similar to Agresti *et al.* [1] we train our network on the synthetic dataset S1 and use the real dataset S3 for validation. In the second stage we use the unlabeled real world dataset S2 in our cyclic self-training procedure for U-DA. We evaluate our method with and without U-DA on the two real world data sets S4, with lower MPI levels but more detailed objects, and S5, a 'box' dataset with higher MPI levels but fewer details. We compare to the Coarse-Fine-Network (CFN), with [1] and without U-DA [2], the DeepToF network [20], the Transient Image Reconstruction network (TIR) [4], and the non-learned

| Method | S4 | | S5 | |
|-------------------------------|-------------|-------------------|-------------|-------------------|
| | MAE [cm] | Relative Error | MAE [cm] | Relative Error |
| ToF (low freq.) | 7.28 | - | 5.06 | - |
| ToF (high freq.) | 5.43 | - | 3.62 | - |
| SRA [8] [†] | 5.11 | 94.1% | 3.37 | 93.1% |
| DeepToF [20] [†] | 5.13 | 70.5%* | 6.68 | 132%* |
| +calibration [2] [†] | 5.46 | 75.0%* | 3.36 | 66.4% |
| TIR [4] [†] | 2.60 | 47.9% | 1.88 | 52.0% |
| CFN [2] [†] | 3.19 | 58.7% | 2.22 | 60.5% |
| + U-DA [1] [†] | 2.36 | 43.5% | 1.66 | 46.1% |
| RADU | 1.83 | 33.7% | 2.59 | 71.5% |
| RADU + U-DA | 2.11 | 38.8% | 1.63 | 45.0% |
| RADU + S-DA | 1.89 | 34.8% | 1.53 | 42.3% |

Table 2. Results of various methods on the real world datasets S4 and S5. Each row reports the MAE and the relative error with respect to the phase unwrapped high frequency ToF depth. (*: relative to low frequency, †: numbers taken from Buratto *et al.* [4])

Sparse Reconstruction Analysis (SRA) [8]. The Mean Absolute Error (MAE) and the remaining relative error are reported in Tab. 2.

The combination of our RADU network with cycled self-training for U-DA outperforms existing approaches on both datasets and successfully removes noise and MPI from the unwrapped ToF depth images, as can be seen in Fig. 6. To additionally evaluate the stability of the cyclic self-training we repeat the fine-tuning of our method 10 times and measured a standard deviation of the MAE at 0.072cm on S4 and 0.021cm on S5, which indicates that the proposed U-DA approach is stable. Interestingly, the performance of our RADU network drops after the domain adaptation on the dataset S4, which we account to the fact that the unlabeled dataset S2 contains ‘box’ scenes, with few details, similar to the ones in S5, whereas S4 contains more complex objects. For comparison, we also report the results of our method after a Supervised Domain Adaptation (S-DA) using the small labeled real world dataset S3 for fine-tuning.

6.2. Experiment 2: Cornell-Box Dataset

We train instances of the previously mentioned CFN, DeepToF and our RADU network on our Cornell-Box dataset described in Sec. 5. Since our dataset contains raw measurements m_θ , we further compare to the End2End network [29]. For a fairer comparison, we perform a hyperparameter tuning for each method, we refer to the supplementary material for details. As our dataset is purely synthetic we do not use domain adaptation strategies.

We evaluate on the test images where our method achieves the lowest MAE of the mentioned methods as can be seen in Tab. 3. The remaining relative error is compa-

| Method | Cornell-Box | | FLAT | |
|------------------|-------------|--------------------------|-------------|-------------------|
| | MAE [cm] | Relative Error | MAE [cm] | Relative Error |
| ToF (low freq.) | 29.0 | - | 59.34 | - |
| ToF (high freq.) | 11.14 | - | - | - |
| DeepToF [20] | 10.17 | 35.1%* | 23.0 | 38.8%* |
| CFN [1,2] | 3.99 | 35.8% [†] | 6.29 | 10.6%* |
| End2End [29] | 5.99 | 53.8% [†] | 6.20 | 10.5%* |
| RADU | 3.64 | 32.7%[†] | 3.31 | 5.58%* |

Table 3. Results of various methods on unseen data from our synthetic Cornell-Box dataset and the FLAT dataset. Each row reports the depth MAE and the relative error with respect to a phase unwrapped ToF depth. (*: relative to low frequency, †: relative to high frequency)

table to the previous experiment, showing that our network, as well as CFN, are able to handle phase wrapping in the input features. The iterative denoising in the latent 3D space in between the three RADU convolutions is shown in Fig. 8.

However, while our method yields better results than the others, objects with low SNR and scenes with high MPI can still lead to failures in the reconstruction, as shown in Fig. 7.

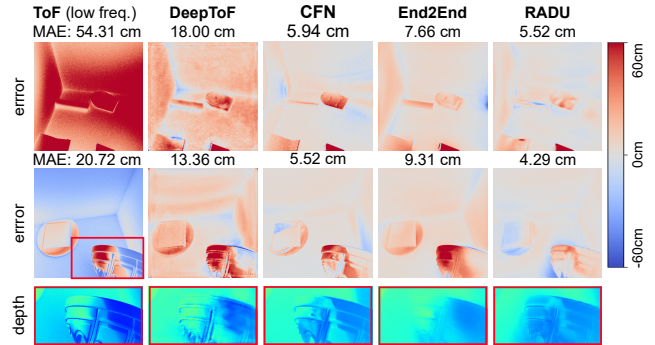


Figure 7. Visual results for two challenging scenes from our Cornell-Box dataset. The top scene contains an object with low SNR at the bottom, where all methods fail to retrieve the correct depth. The bottom scene exhibits high MPI, and shows a failure case of our method, where the object boundaries are blurred.

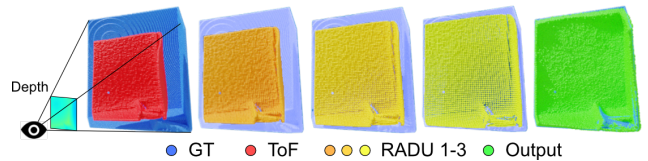


Figure 8. Visualization of the latent point clouds on a corner scene. The depth reconstruction improves after every RADU layer.

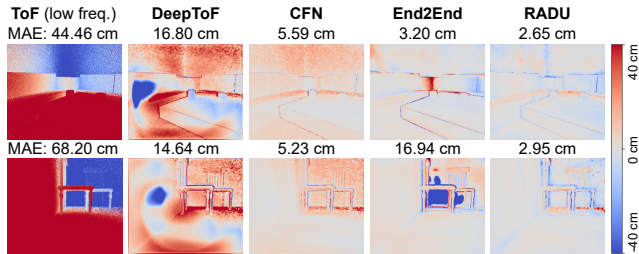


Figure 9. Depth maps on the FLAT dataset. The top row shows an example where both RADU and End2End produce an almost noise free prediction. The bottom row shows a failure case of End2End.

6.3. Experiment 3: FLAT Dataset

In a third experiment we train our method on the FLAT dataset which contains nine raw correlations for three frequencies, simulating the Kinect2 ToF sensor. Unlike in the previous cases the low frequency signal is non-sinusoidal [10] which introduces additional distortions in the depth estimation using Eq. (6). A further challenge is the domain gap between the training data, which to a large part consists of images of isolated floating objects and thus low MPI levels, while the test data contains complete scenes.

We compare our method to the same learned methods as in the previous experiment, again performing a hyperparameter search for each method.

We evaluate on the 120 test images, where our method achieves the lowest MAE compared to the other learned methods, see Tab. 3. In Fig. 9 we show error images for the different methods. We recognize that End2End can produce competitive results in some cases but has a tendency to create artifacts, which we assume to stem from the domain gap between training and test data.

6.4. Ablation: Latent 3D Representation

To validate the benefits of our 3D RADU convolutions we evaluate the performance when replacing the RADU convolutions with 2D, 2.5D or 3D point convolutions. In detail we compare to 2.5D convolutions [35], which performs three 2D convolutions on separate depth ranges, KPConv [30] which uses spherical kernel points to represent the 3D kernel function, MConv [13], which uses kernel MLPs and a density estimation, and PointConv [32] which uses a kernel MLP with a learned density estimation. We conduct a smaller experiment without domain adaption, using S1 for training and S3 for validation. For a fair comparison we conduct a hyperparameter search for each method, and report results of the validation MAE in Tab. 4.

The results show that latent 3D information can help to improve the performance, but the choice of the convolution type is critical. Both the 2.5D convolution and MConv yield better results than the 2D convolution, on both train-

| Method | Training (S1) MAE [cm] | Validation (S3) MAE [cm] |
|-------------------|---------------------------|-----------------------------|
| 2D Conv | 9.68 | 2.72 |
| 2.5D Conv [35] | 8.79 | 2.61 |
| 3D KPConv [30] | 10.86 | 4.00 |
| 3D PointConv [32] | 10.49 | 3.42 |
| 3D MConv [13] | 8.38 | 2.51 |
| 3D MConv + RADU | 7.87 | 2.28 |

Table 4. Results of our network architecture with different layer types in the latent block. We report MAE on training (synthetic) and validation (real) data after hyperparameter optimization.

ing and validation data, outperformed only by our proposed RADU extension of the MConv layer.

7. Limitations

While we covered several error sources present in ToF data in our experiments, we did not investigate motion artifacts that occur in dynamic scenes [12], which would require additional considerations in the network architecture as shown in previous works [10, 26]. However, we believe that the latent denoised 3D point cloud representation of our network can potentially be used to improve image alignment. Further, the results on our Cornell-Box dataset indicate that high MPI, low SNR and fine details can have a drastic impact in the depth estimation, not only for our method but for all evaluated methods. Finally learned methods, including ours, are trained for specific sensor data and are thus not able to generalize to for example different modulation frequencies. We believe learned methods which are able to treat sensor properties as input parameters, as in traditional approaches [8], is a promising line of research.

8. Conclusion

In this paper we presented an extension of unstructured 3D convolutions for ToF denoising, which exploits structured information from depth images to iteratively denoise the point cloud in 3D space. The experiments indicate that latent 3D representations improve the denoising capabilities of neural networks for various error sources present in ToF data. Further, we demonstrated that cyclic self-training using pseudo-labels on real data can effectively be used for unsupervised domain adaptation on ToF data and, applied to our network, outperforms existing methods on two real world data sets.

While we demonstrated our RADU layers in the context of ToF denoising, they can in principle be applied to any task where 2.5D information is present, in order to benefit from both a latent 3D representation and an iterative denoising of the former.

9. Acknowledgements

This project is financed by the Baden-Württemberg Stiftung gGmbH. We thank Julio Marco for his information on adapting the transient renderer, and Markus Miller and Rainer Michalzick for their insights on the ToF working principle and noise simulation.

References

- [1] Gianluca Agresti, Henrik Schaefer, Piergiorgio Sartor, and Pietro Zanuttigh. Unsupervised domain adaptation for ToF data denoising with adversarial learning. In *Proceedings of the IEEE/CVF Conference on Computer Vision and Pattern Recognition*, pages 5584–5593, 2019. 1, 2, 5, 6, 7, 13
- [2] Gianluca Agresti and Pietro Zanuttigh. Deep learning for multi-path error removal in ToF sensors. In *Proceedings of the European Conference on Computer Vision (ECCV) Workshops*, September 2018. 1, 2, 5, 6, 7
- [3] European Machine Vision Association et al. Standard for characterization of image sensors and cameras. *EMVA Standard*, 1288, 2010. 12
- [4] Enrico Buratto, Adriano Simonetto, Gianluca Agresti, Henrik Schäfer, and Pietro Zanuttigh. Deep learning for transient image reconstruction from ToF data. *Sensors*, 21(6):1962, 2021. 1, 2, 6, 7
- [5] Yan Chen, Keyuan Qian, Xuanye Cheng, and Jingkun Zhou. A learning method to optimize depth accuracy and frame rate for time of flight camera. In *IOP Conference Series: Materials Science and Engineering*, volume 563, page 042067. IOP Publishing, 2019. 2
- [6] Yan Chen, Jimmy Ren, Xuanye Cheng, Keyuan Qian, Luyang Wang, and Jinwei Gu. Very power efficient neural time-of-flight. In *Proceedings of the IEEE/CVF Winter Conference on Applications of Computer Vision*, pages 2257–2266, 2020. 2
- [7] Mario Frank, Matthias Plaue, Holger Rapp, Ullrich Köthe, Bernd Jähne, and Fred A Hamprecht. Theoretical and experimental error analysis of continuous-wave time-of-flight range cameras. *Optical Engineering*, 48(1):013602, 2009. 3, 11
- [8] Daniel Freedman, Yoni Smolin, Eyal Krupka, Ido Leichter, and Mirko Schmidt. SRA: Fast removal of general multipath for ToF sensors. In *European Conference on Computer Vision*, pages 234–249. Springer, 2014. 7, 8
- [9] Cindy M Goral, Kenneth E Torrance, Donald P Greenberg, and Bennett Battaile. Modeling the interaction of light between diffuse surfaces. *ACM SIGGRAPH computer graphics*, 18(3):213–222, 1984. 6, 12
- [10] Qi Guo, Iuri Frosio, Orazio Gallo, Todd Zickler, and Jan Kautz. Tackling 3D ToF artifacts through learning and the FLAT dataset. In *The European Conference on Computer Vision (ECCV)*, September 2018. 1, 2, 6, 8, 12
- [11] Felipe Gutierrez-Barragan, Huaijin Chen, Mohit Gupta, Andreas Velten, and Jinwei Gu. iToF2dToF: A robust and flexible representation for data-driven time-of-flight imaging. *arXiv preprint arXiv:2103.07087*, 2021. 1, 2
- [12] Miles Hansard, Seungkyu Lee, Ouk Choi, and Radu Patrice Horaud. *Time-of-flight cameras: principles, methods and applications*. Springer Science & Business Media, 2012. 1, 3, 8, 11
- [13] Pedro Hermosilla, Tobias Ritschel, Pere-Pau Vázquez, Àlvar Vinacua, and Timo Ropinski. Monte carlo convolution for learning on non-uniformly sampled point clouds. *ACM Transactions on Graphics (TOG)*, 37(6):1–12, 2018. 1, 3, 4, 8, 11
- [14] Geoffrey Hinton, Oriol Vinyals, and Jeff Dean. Distilling the knowledge in a neural network. *arXiv preprint arXiv:1503.02531*, 2015. 2
- [15] Adrian Jarabo, Julio Marco, Adolfo Muñoz, Raul Buisan, Wojciech Jarosz, and Diego Gutierrez. A framework for transient rendering. *ACM Transactions on Graphics (SIGGRAPH Asia 2014)*, 33(6), 2014. 12, 15
- [16] Diederik P Kingma and Jimmy Ba. Adam: A method for stochastic optimization. *arXiv preprint arXiv:1412.6980*, 2014. 13
- [17] Ananya Kumar, Tengyu Ma, and Percy Liang. Understanding self-training for gradual domain adaptation. In *International Conference on Machine Learning*, pages 5468–5479. PMLR, 2020. 2, 5
- [18] Dong-Hyun Lee et al. Pseudo-label: The simple and efficient semi-supervised learning method for deep neural networks. In *Workshop on challenges in representation learning, ICML*, volume 3, page 896, 2013. 2, 5
- [19] Hong Liu, Jianmin Wang, and Mingsheng Long. Cycle self-training for domain adaptation. *arXiv preprint arXiv:2103.03571*, 2021. 2, 5
- [20] Julio Marco, Quercus Hernandez, Adolfo Munoz, Yue Dong, Adrian Jarabo, Min H Kim, Xin Tong, and Diego Gutierrez. DeepToF: off-the-shelf real-time correction of multipath interference in time-of-flight imaging. *ACM Transactions on Graphics (ToG)*, 36(6):1–12, 2017. 1, 2, 6, 7, 12, 13
- [21] Alexander Mey and Marco Loog. A soft-labeled self-training approach. In *2016 23rd International Conference on Pattern Recognition (ICPR)*, pages 2604–2609. IEEE, 2016. 2
- [22] Markus Miller, Hongwang Xia, Mina Beshara, Susanne Menzel, Karl Joachim Ebeling, and Rainer Michalzick. Large-area transmission modulators for 3d time-of-flight imaging. In *Unconventional Optical Imaging II*, volume 11351, page 113511F. International Society for Optics and Photonics, 2020. 6, 12
- [23] Thu Nguyen-Phuoc, Chuan Li, Lucas Theis, Christian Richardt, and Yong-Liang Yang. Hologan: Unsupervised learning of 3d representations from natural images. In *Proceedings of the IEEE/CVF International Conference on Computer Vision*, pages 7588–7597, 2019. 2
- [24] Mary A Pagnutti, Robert E Ryan, Maxwell J Gold, Ryan Harlan, Edward Leggett, James F Pagnutti, et al. Laying the foundation to use raspberry pi 3 v2 camera module imagery for scientific and engineering purposes. *Journal of Electronic Imaging*, 26(1):013014, 2017. 12
- [25] Viraj Prabhu, Shivam Khare, Deeksha Kartik, and Judy Hoffman. Sentry: Selective entropy optimization via committee consistency for unsupervised domain adaptation. In

- Proceedings of the IEEE/CVF International Conference on Computer Vision*, pages 8558–8567, 2021. 2
- [26] Di Qiu, Jiahao Pang, Wenxiu Sun, and Chengxi Yang. Deep end-to-end alignment and refinement for time-of-flight RGB-D module. In *Proceedings of the IEEE/CVF International Conference on Computer Vision*, pages 9994–10003, 2019. 2, 8
- [27] Kilho Son, Ming-Yu Liu, and Yuichi Taguchi. Learning to remove multipath distortions in time-of-flight range images for a robotic arm setup. In *2016 IEEE International Conference on Robotics and Automation (ICRA)*, pages 3390–3397. IEEE, 2016. 1, 2
- [28] Seongjong Song and Hyunjung Shim. Depth reconstruction of translucent objects from a single time-of-flight camera using deep residual networks. In *Asian Conference on Computer Vision*, pages 641–657. Springer, 2018. 1, 2
- [29] Shuochen Su, Felix Heide, Gordon Wetzstein, and Wolfgang Heidrich. Deep end-to-end time-of-flight imaging. In *Proceedings of the IEEE Conference on Computer Vision and Pattern Recognition*, pages 6383–6392, 2018. 1, 2, 7, 13
- [30] Hugues Thomas, Charles R. Qi, Jean-Emmanuel Deschaud, Beatriz Marcotequi, François Goulette, and Leonidas J. Guibas. KPConv: Flexible and deformable convolution for point clouds. *Proceedings of the IEEE International Conference on Computer Vision*, 2019. 3, 8
- [31] Yan Wang, Wei-Lun Chao, Divyansh Garg, Bharath Hariharan, Mark Campbell, and Kilian Q Weinberger. Pseudolidar from visual depth estimation: Bridging the gap in 3d object detection for autonomous driving. In *Proceedings of the IEEE/CVF Conference on Computer Vision and Pattern Recognition*, pages 8445–8453, 2019. 2
- [32] Wenxuan Wu, Zhongang Qi, and Li Fuxin. PointConv: Deep convolutional networks on 3D point clouds. In *Proceedings of the IEEE/CVF Conference on Computer Vision and Pattern Recognition*, pages 9621–9630, 2019. 8
- [33] Lingzhu Xiang, Florian Echtler, Christian Kerl, Thiemo Wiedemeyer, Lars Hanyazou, Ryan Gordon, Francisco Facioni, laborer2008, Rich Wareham, Matthias Goldhoorn, alberth, gaborpapp, Steffen Fuchs, jmtatsch, Joshua Blake, Federico, Henning Jungkurth, Yuan Mingze, vinouz, Dave Coleman, Brendan Burns, Rahul Rawat, Serguei Mokhov, Paul Reynolds, P.E. Viau, Matthieu Fraissinet-Tachet, Ludique, James Billingham, and Alistair. libfreenect2: Release 0.2, Apr. 2016. 2
- [34] Sang Michael Xie, Ananya Kumar, Robbie Jones, Fereshte Khani, Tengyu Ma, and Percy Liang. In-n-out: Pre-training and self-training using auxiliary information for out-of-distribution robustness. *arXiv preprint arXiv:2012.04550*, 2020. 2
- [35] Yajie Xing, Jingbo Wang, Xiaokang Chen, and Gang Zeng. 2.5D convolution for RGB-D semantic segmentation. In *2019 IEEE International Conference on Image Processing (ICIP)*, pages 1410–1414. IEEE, 2019. 2, 8
- [36] Qingnan Zhou and Alec Jacobson. Thingi10k: A dataset of 10,000 3d-printing models. *arXiv preprint arXiv:1605.04797*, 2016. 12
- [37] Yang Zou, Zhiding Yu, BVK Kumar, and Jinsong Wang. Unsupervised domain adaptation for semantic segmentation via class-balanced self-training. In *Proceedings of the European conference on computer vision (ECCV)*, pages 289–305, 2018. 2
- [38] Yang Zou, Zhiding Yu, Xiaofeng Liu, BVK Kumar, and Jinsong Wang. Confidence regularized self-training. In *Proceedings of the IEEE/CVF International Conference on Computer Vision*, pages 5982–5991, 2019. 2

A. Further Insights on ToF Working Principle

A convenient formulation for the sinusoidal part v of the measurements m_θ , is to represent it in the complex plane \mathbb{C} via

$$v = A \cdot e^{i\Delta\varphi}, \quad (12)$$

$$Re(v) = \sum_{\theta} -\sin(\theta) \cdot m_\theta, \quad (13)$$

$$Im(v) = \sum_{\theta} \cos(\theta) \cdot m_\theta. \quad (14)$$

Which allows to express the measurements m_θ as [7]

$$m_\theta = I + A \cos(\Delta\varphi + \theta), \quad (15)$$

$$= I + Re(v \cdot e^{i\theta}), \quad (16)$$

Using this notation the amplitude A , the intensity I and the the phase delay $\Delta\varphi$ can be recovered as

$$A = \|v\|_2. \quad (17)$$

$$I = \frac{1}{N} \sum_{\theta} m_\theta, \quad (18)$$

$$\Delta\varphi = \arg(v) \quad (19)$$

$$= \arctan\left(\frac{Re(v)}{Im(v)}\right), \quad (20)$$

where N is the number of phase shifted measurements m_θ . Note that this is not an exact solution but a least-squares optimal solution [7].

Given measurements at two different frequencies f_1, f_2 a computationally cheap solution [12] to unwrap the distances is by minimizing

$$\min_{m,n} |d(f_1) + m \cdot d_{max}(f_1) - d(f_2) + n \cdot d_{max}(f_2)|. \quad (21)$$

We use this approach to compute the phase unwrapped high frequency ToF depth in the experiment on our Cornell-Box dataset.

B. Extension of MC-Convolutions with RADU

Monte-Carlo Convolution The Monte-Carlo point convolution of Hermosilla *et al.* [13] approximates the convolution of two continuous functions, the features f and the kernel function g , where f is only known at the discrete positions $\{p_i\}$, the point cloud, using the Monte-Carlo numerical integration. Formally, let a point cloud $\{p_i^{in}\} \subset \mathbb{R}^3$, input features $\{f_i^{in}\} \subset \mathbb{R}^{C_{in}}$ and a convolution radius $r \in \mathbb{R}$ be given. Further let \mathcal{N}_j denote the neighborhood of p_j^{in} , given as

$$\mathcal{N}_j = \{i : \|p_j - p_i\|_2 \leq r\} \subset \mathbb{N}. \quad (22)$$

Then the Monte-Carlo convolution on point p_j with radius r is defined as

$$(f * g)(p_j) := |\mathcal{N}_j|^{-1} \sum_{i \in \mathcal{N}_j} \frac{f_i \cdot g\left(\frac{p_i - p_j}{r}\right)}{pde(p_i | p_j)}, \quad (23)$$

where $pde(p_i | p_j)$ denotes a point-density estimation of p_i inside the receptive field of p_j , and the kernel function $g : \mathbb{R}^3 \rightarrow \mathbb{R}^{C_{in} \times C_{out}}$ is represented implicitly using one or multiple MLPs. In analogy to 2D convolutions, the evaluation of g on the relative position $(p_i - p_j)/r$ yields the convolution weight matrix W_{ij} .

RADU To predict the additional point update $p_j^u \in \mathbb{R}$ we extend g to predict an additional output channel, *i.e.*

$$g : \mathbb{R}^3 \rightarrow \mathbb{R}^{C_{in} \times C_{out}} \times \mathbb{R}^{C_{in} \times 1} \\ \simeq \mathbb{R}^{C_{in} \times (C_{out} + 1)}, \quad (24)$$

$$\frac{p_i - p_j}{r} \mapsto (W_{ij}, W_{ij}^u). \quad (25)$$

Using this kernel function in Eq. (23), the dimensionality of the output of the convolution is increased by one, *i.e.* $(f * g)(p_j) \in \mathbb{R}^{C_{out} + 1}$. We split the output into features $f_j^{out} \in \mathbb{R}^{C_{out}}$, and the point update p_j^u . To summarize the point update is computed as

$$p_j^u := |\mathcal{N}_j|^{-1} \sum_{i \in \mathcal{N}_j} \frac{f_i \cdot W_{ij}^u}{pde(p_i | p_j)}. \quad (26)$$

The final update along the associated camera ray is performed as described in the main paper

$$p_j^{out} = p_j^{in} + \alpha \cdot \tanh(p_j^u) \cdot r_j. \quad (27)$$

C. Network Architecture - Hyperparameters

We provide additional parameters of our network architecture for a full description. Our networks consists of three initial 2D convolutions, followed by a 2.5D pooling layer, three 3D RADU convolutions, a 3D-2D projection with up-scaling and a final stack of three 2D convolutions.

The first three 2D convolutions have feature channels of sizes [64, 64, 128]. The 2.5D pooling layer uses a stride of 8×8 and applies average pooling on both the point depths and the features. The 3D RADU convolutions use single MLPs with 16 hidden neurons as kernel functions, and a regularization of the point updates with $\alpha = 0.1$ m. The receptive fields are [0.1 m, 0.2 m, 0.4 m] and the feature channels are of sizes [128, 256, 128]. The up-scaling layer uses bilinear interpolation. The extracted depth of the points is projected back into a 2D depth image and is used as additional input to the following 2D layers. The final 2D convolutions have feature channels of sizes [64, 64, 1].

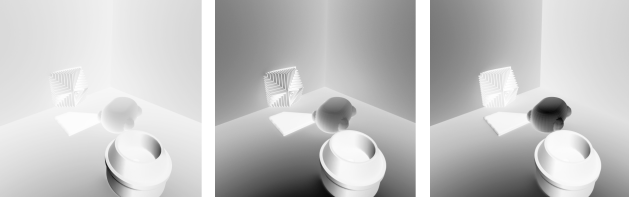


Figure 10. An example scene with three different material properties. The images show the intensity I at a frequency of 20 MHz as given by Eq. (18). In the left scene the box material is highly reflective, the right scene contains an object with a dark material.

In between all convolutional layers, 2D and 3D, we use leaky ReLU with $\alpha = 0.1$ as non-linear activation. All 2D convolutions further have a kernel size of 3×3 and use 'same' padding.

Finally we use a skip connection between the two 2D blocks with feature concatenation.

D. Cornell-Box - Dataset Generation

We generate our dataset using the transient renderer of Jarabo *et al.* [15], which has been deployed for ToF data generation in previous works [10, 20].

Camera Properties Inspired by the work of Miller *et al.* [22], which propose an approach to modify standard cameras for ToF captures, we simulate the properties of a Raspberry Pi 3 camera equipped with an Electro-Absorption Modulator (EAM), which modulates the received signal s_r in front of the camera sensor.

Scene Generation To ensure challenging scenes with high MPI levels we design our scenes inspired by the Cornell-Box [9] layout, and place a random number of objects, between 1 and 10, in the scene. The used objects meshes are taken from a subset of the Thingi10k dataset [36], containing 3D models under CC license. For each 3D object a material property is randomly sampled, the assignment of dark materials allows to simulate regions with lower SNR values. Further the material of the surrounding box allows, to some degree, control over the level of MPI in the scene. An example of a scene with different materials is shown in Fig. 10.

ToF Simulation Using the transient renderer we compute the impulse response $h(t)$ of the scene, which contains the received signal s_r in a time resolved format after illuminating the scene with a light impulse. Given the impulse response the measurements m_θ can be simulated for different frequencies f and phase offsets θ using

$$s_r(t) = h(t) * s_e(t), \quad (28)$$

in the formula from the main paper

$$m_\theta = \frac{1}{\delta t} \int_{\delta t} s_r(t) \cdot s_e \left(t + \frac{\theta}{2\pi f} \right) dt. \quad (29)$$

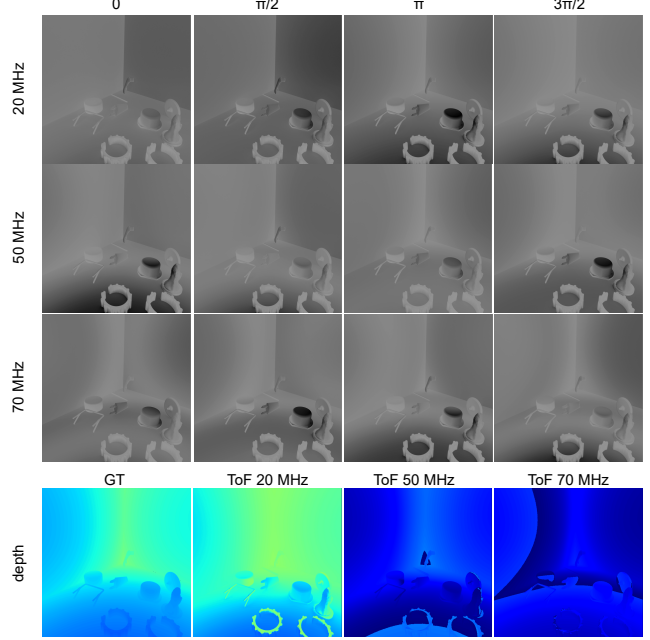


Figure 11. Example scene from our Cornell-Box dataset. Simulated measurements m_θ for different values of $\theta \in \{0, \pi/2, \pi, 3\pi/2\}$ and frequencies $f \in \{20, 50, 70\}$ are shown in the top rows. The reconstructed ToF depths, including phase wrapping, are shown in the bottom row.

The resulting measurements for an example scene are shown in Fig. 11. Further a scene table can be found at the end of this document in Fig. 21, 22 and 23.

Additional Noise We simulate the combination of shot noise, thermal noise and read noise as an Additive White Gaussian Noise (AWGN) using the specifications of the Raspberry Pi 3 camera of Pagnutti *et al.* [24], who use the linear noise model of the EMVA Standard 1288 [3]. We use the ISO 100 measurements of the former as reference, who measured a gain K of 0.33 and a Y-intercept b of -18.4 on the mean-variance curves

$$\sigma^2 = K \cdot m + b, \quad (30)$$

where m is the mean value across multiple measurements and σ^2 is the variance of the measurements. From Eq. (30) we infer the pixel-wise variance $\sigma_{x,y}^2$ dependent on the measurement m_θ on pixel (x, y) for the AWGN $\mathcal{N}(0, \sigma_{x,y}^2)$.

In our dataset, we provide measurements m_θ without the AWGN to allow the online generation of AWGN during training for data augmentation, and to allow future researchers to simulate other noise models.

E. Experiments

We briefly describe additional details about the experiments, including data augmentation and hyperparameter settings.

The ADAM optimizer [16] is used during backpropagation in all trainings described below.

E.1. Data Augmentation

To increase the variety in the datasets we use the following data augmentation strategies on the input features.

Mirroring Random mirroring along image axes.

Image Rotation Random rotation by $0^\circ, 90^\circ, 180^\circ, 270^\circ$.

Small Rotation Additional rotation with a random angle in the range $[-5^\circ, 5^\circ]$. Values outside the image boundaries are interpolated with a *nearest* strategy, as implemented in the preprocessing pipeline of `tensorflow.keras`.

Noise Additive Gaussian noise with a relative standard deviation of 0.02.

Random Cropping In the case of training on image patches we crop random regions of the images every epoch.

We further experimented with the MPI augmentation of Agresti *et al.* [1], but found it did not improve the performance in our experiments.

E.2. Soft-Kinect - Datasets S1-S5

Since no raw measurements are available in the dataset, we do not compare to the End2End method in this setting. While in theory a reconstruction of m_θ could be done using Eq. (15), the error accumulation results in data unfit for training.

The input resolution of the Soft-Kinect is 320×240 , which results in a latent point cloud of $1.2k$ points after the 2.5D pooling in our proposed network architecture. On the real datasets of size 320×239 we pad the input to the using reflective padding to the full resolution 320×240 .

We use the same input features as CFN, by setting $f_1 = 70\text{MHz}$, $f_2 = 20\text{MHz}$, $f_3 = 40\text{MHz}$. Note, the provided ToF depth at 70MHz is phase unwrapped in this experiment. **Pre-Training** Our network is pre-trained on the synthetic dataset S1 using a learning rate of $1e-3$ and an exponential learning rate decay of 0.1 every 100 epochs and a batch size of 8. The network converged after 300 epochs.

Cyclic Self-Training After pre-training our network on synthetic data, we train the network on the unlabeled real dataset S2 using pseudo-labels as described in the main paper. In each training step, we choose real examples with a probability of $p = 0.5$ and update the pseudo-labels every $n_{cycle} = 20$ epochs. We train with a small learning rate of $5e-5$ and a batch size of 4 for 100 epochs.

Supervised Domain Adaptation For comparison we fine-tune our network, after pre-training on synthetic data, using the labeled real dataset S3. We train with a small learning rate of $1e-5$ and a batch size of 4 for 100 epochs.

E.3. RaspBerry-Pi 3 - Cornell-Box Dataset

We use a resolution of 512×512 during training which results in 4096 points in the latent point clouds. The in-

put features for our network are computed by using $f_1 = 20\text{MHz}$, $f_2 = 50\text{MHz}$, $f_3 = 70\text{MHz}$. The network is trained with an initial learning rate of $1e-3$ and an exponential learning rate decay of 0.1 every 100 epochs, and a batch size of 4. The network converged after 300 epochs.

DeepToF includes an Auto-Encoder (AE) training stage on real data for domain adaptation. As there is no real data in this experiment, we train models with pre-training the AE, as described in the original paper, and training the entire network combined, without pre-training. We also tune the learning rate with initial learning rates from $\{1e-3, 1e-4\}$ and decay steps from $\{50, 75, 100\}$. The learning rate in the AE stage is set constant at $1e-4$ for 15 epochs, as suggested in the original paper [20]. The learning rate decay is not fully specified in the original paper, we assume a decay of 0.1 every 75 epochs, which matches the authors description. We use an L2-Loss, a batch size of 16, and the low frequency 20MHz ToF-depth as input as in the original paper.

CFN was investigated in two papers, we use the more recent version [1] as reference for our experiments, which predicts the depth directly and does not use additional filtering algorithms. As no real data is available we drop the unsupervised adversarial part of the training, as with our network architecture. The original paper [1] used a fixed learning rate of $5e-6$. We investigate the static learning rates $\{1e-4, 1e-5, 5e-6\}$ and also in combination with a learning rate decay after $\{100, 150\}$ epochs. We use a coarse-fine L1-loss and a batch size of 4 as in the original paper [1]. The input features for CFN are the same as for our network.

End2End predicts depths directly from raw correlations, using a generative approach, which we also incorporate into our trainings. The original network uses a static learning rate of $5e-4$ for 50 epochs before decaying the learning rate linearly to zero for 100 epochs [29]. We additionally investigate using exponential learning rate decays with initial learning rates from $\{5e-4, 5e-3\}$ at decay steps from $\{50, 100\}$. We further use the combination of adversarial, total-variation and L1-loss of the original paper. The first two raw measurements at phase offsets $0, \pi/2$ of the two higher frequencies 60MHz, 70MHz are used as input.

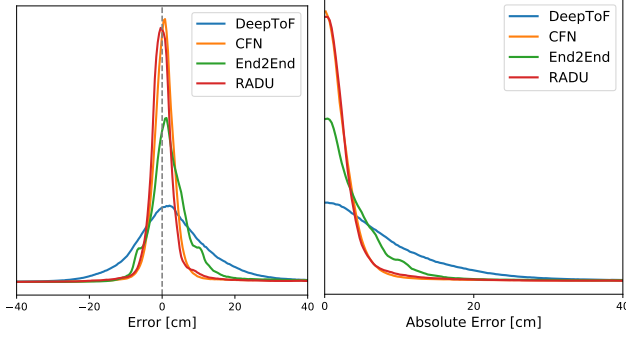
We also investigate the influence of training on image patches of resolution 128×128 , as used by CFN and End2End originally. During training we ensure that the cropped images inside a batch are from different scenes.

We compare the resulting MAE on the validation set after tuning and using the original hyperparameters (vanilla):

| | DeepToF | CFN | End2End |
|---------|---------|------|---------|
| vanilla | 11.97 | 4.72 | 9.14 |
| tuned | 10.10 | 3.83 | 8.19 |

The hyperparameters after tuning are:

DeepToF: LR $5e-4$, decay 0.1 every 100 epochs, AE pre-



| Method | Median | σ |
|---------|--------------|-------------|
| DeepToF | 2.27 | 15.61 |
| CFN | 0.42 | 8.80 |
| End2End | 1.72 | 14.97 |
| RADU | -0.28 | 7.64 |

Figure 12. Error distributions with median and standard deviation σ of the examined networks on our Cornell-Box dataset. An optimal distribution would be a single peak at 0. Both CFN and RADU have a similar distribution, where the median and standard deviation of CFN are slightly worse.

training, full resolution.

CFN: LR $1e-4$, decay 0.1 every 100 epochs, on patches.

End2End: $5e-4$, decay: 0.1 every 100 epochs, full resolution.

Error distributions and statistical values are compared in Fig. 12.

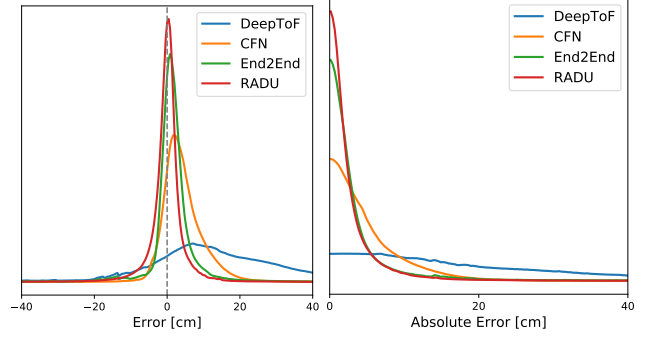
E.4. Kinect2 - FLAT Dataset

The FLAT dataset contains raw measurements simulating a Kinect2 camera for sinusoidal modulations at frequencies at 40MHz and ~ 58.8 MHz, and for a non-sinusoidal modulation at ~ 30.3 MHz. For each modulation three measurements were performed for phase offsets with a spacing of approximately $2\pi/3$.

The resolution of the Kinect2 is 424×512 which results in 3392 points in the latent point clouds of our network. We train our network with an initial learning rate of $1e-3$ and an exponential learning rate decay of 0.3 every 100 epochs, and a batch size of 2. The network converged after 600 epochs.

For DeepToF we use the low frequency ToF-depth as input. For CFN and our network we compute the input features using $f_1 = 30.3$ MHz, $f_2 = 40$ MHz, $f_3 = 58.8$ MHz. For End2End we use the first two raw measurements of the two higher frequencies 40MHz, 58.8MHz as input.

We perform the same hyper parameter tuning as in the previous section and achieve the following MAE on the validation set:



| Method | Median | σ |
|---------|--------------|-------------|
| DeepToF | 12.19 | 33.08 |
| CFN | 3.22 | 19.08 |
| End2End | 1.07 | 25.55 |
| RADU | -0.08 | 7.83 |

Figure 13. Error distributions with median and standard deviation σ of the examined networks on the FLAT dataset. An optimal distribution would be a single peak at 0.

| | DeepToF | CFN | End2End |
|---------|---------|------|---------|
| vanilla | 11.52 | 4.30 | 6.21 |
| tuned | 8.66 | 3.57 | 5.90 |

The hyperparameters after tuning are:

DeepToF: LR: $1e-3$, decay: 0.1 every 50 epochs, combined training, on patches.

CFN: static LR: $1e-4$, on patches.

End2End: LR: $5e-4$, decay: 0.1 every 100 epochs, full resolution.

Error distributions and statistical values are compared in Fig. 13.

Code optimizations for FLAT dataset. The synthetic data used for training in the FLAT dataset contains a high ratio of background pixels, which we masked in the loss functions during training.

When training on patches we ensure to have non-empty images inside the batches.

As the background pixels are associated with depth 0, they are all projected to the same point $\vec{0} \in \mathbb{R}^3$. This introduces a heavy memory usage in 3D convolutions as these identical points are all considered as neighbors to each other.

To reduce the memory impact we apply a filter during training, which drops all masked points in the 3D projection $\mathcal{P}_{C \rightarrow G}$, which results in a varying number of points per image. After the 3D block of our network the points are projected back into 2D by ordering the points in a grid using a sparse data format with pixel ids inferred from the masking.

F. Ablations

We provide additional information about the ablation from the main paper and an additional ablation on the hyperparameter α in our RADU convolutions.

F.1. Ablation 1: Latent 3D Representation

For the 2D and 3D variants of our network architecture we use the same number of features in the 3D bottleneck block, namely $[128, 256, 128]$. For the 2.5D convolutions, which performs 3 convolutions for foreground, neighborhood and background, we change the feature dimensions to $[129, 258, 129] = [3 \cdot 43, 3 \cdot 86, 3 \cdot 43]$, in order to make them divisible by 3.

The neighborhood radii are equal for all 3D convolutions at $[0.1m, 0.2m, 0.4m]$, for the 2D convolutions we use pixel neighborhoods of $[3, 5, 9]$, which is equal to doubling the pixel L0-distances $[1, 2, 4]$. For the 2.5D convolutions we use a fixed neighborhood size of 3 pixels, as larger kernels were too demanding in memory consumption.

We use the following additional hyperparameters for the 3D convolutions:

KPConv: 15 kernel points.

PointConv: 16 hidden units in the kernel MLP.

MCCConv: 1 kernel MLP with 16 hidden units.

We train all variants with different hyperparameters and choose the run which achieved the best validation loss. The initial learning rate is chosen from $\{1e-2, 1e-3, 1e-4\}$ and decayed with an exponential learning rate decay with rates $\{0.1, 0.3\}$ every $\{50, 100, 150\}$ epochs. The following settings achieved the best validation MAE on S3:

| type | init LR | decay rate | decay steps |
|-----------|---------|------------|-------------|
| 2D | 1e-2 | 0.1 | 100 |
| 2.5D | 1e-3 | 0.1 | 100 |
| KPConv | 1e-3 | 0.3 | 150 |
| PointConv | 1e-3 | 0.1 | 150 |
| MCCConv | 1e-3 | 0.3 | 100 |

F.2. Ablation 2: Hyperparameter α

As discussed in the main paper the RADU layers receive direct gradients from the coarse loss, which can increase the risk of overfitting. We investigate the influence of the regularization hyperparameter α of the RADU layer, and train instances of our network, again using S1 and S3, for different values of α , including a dynamic value choice, by using the convolution radius $\alpha_l = r_l$, in our case 0.1 m, 0.2 m, and 0.4 m. Results are reported in Tab. 5. While the result indicate that a wrong choice of α yields the risk of overfitting on the training data, we found that $\alpha = 0.1$ m leads to good performance on the three datasets of the main paper.

| α [m] | Training (S1) MAE [cm] | Validation (S3) MAE [cm] |
|-----------------|---------------------------|-----------------------------|
| 0.0 | 8.38 | 2.51 |
| 0.1 | 7.87 | 2.28 |
| 0.2 | 7.51 | 2.81 |
| 1.0 | 6.93 | 3.42 |
| r | 7.48 | 2.45 |

Table 5. Influence of the hyperparameter α in the RADU convolutions. We report MAE on training (synthetic) and validation (real) data. The case $\alpha = r$ uses the receptive field r as scale. The value $\alpha = 0$ corresponds to a standard MCCConv layer.

G. Implementation

All network implementations were done in TensorFlow 2.3.0-gpu and Python 3.6. The dataset generation was done using Python 3.6 and the transient renderer of Jarabo *et al.* [15] in version 26 February 2019 - Release v1.2.

H. Qualitative Results

H.1. Cornell-Box Dataset

We show predictions for one view point per scene in Fig. 15, 16, 17 and 18.

We further show a larger version of Figure 8 of the main paper in Fig. 14, which shows the iterative denoising on the latent point clouds.

H.2. FLAT Dataset

We show predictions for a subset of the images in the dataset in Fig. 19 and 20.

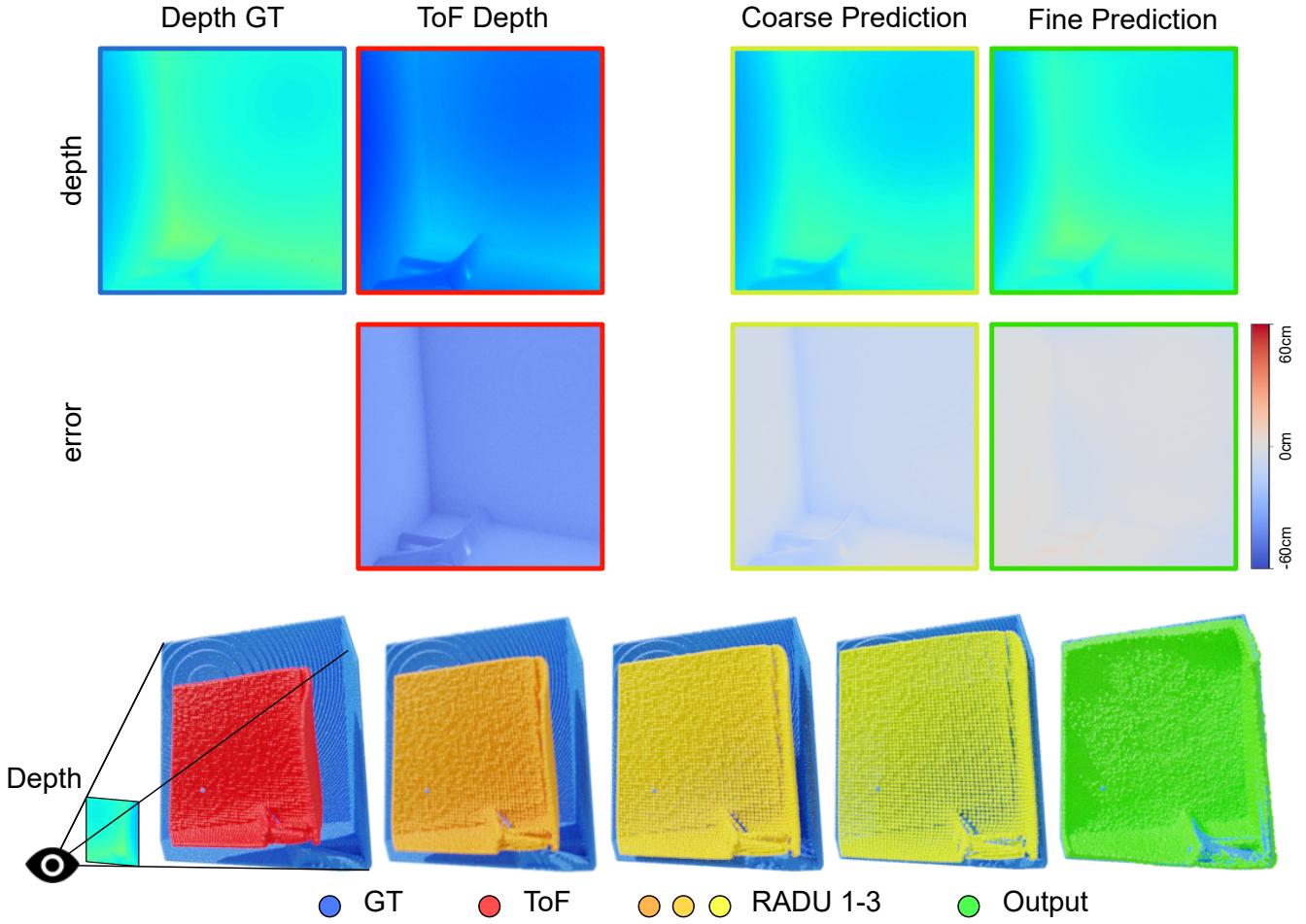


Figure 14. Larger version of Figure 8 in the main paper. The top row shows depth and error maps, the bottom row shows the point clouds in 3D space. The initial ToF depth reconstruction (red) is far from the ground truth depth (blue). After each RADU convolution the latent point clouds (orange to yellow) move closer to the correct depth. The final latent point cloud (yellow) already yields a good coarse reconstruction of the scene, which is further refined in the 2D block of the network (green).

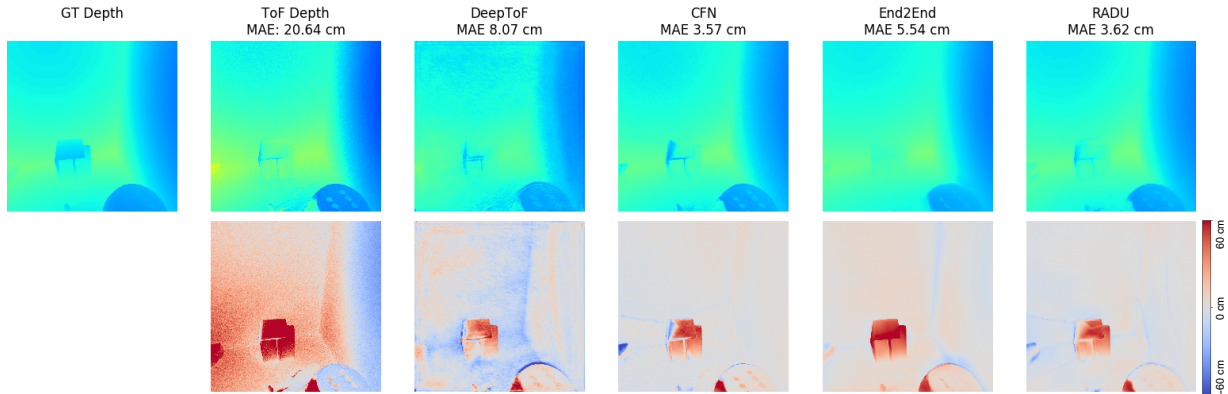


Figure 15. Results on the Cornell-Box Dataset. First row shows depths, second row shows error maps.

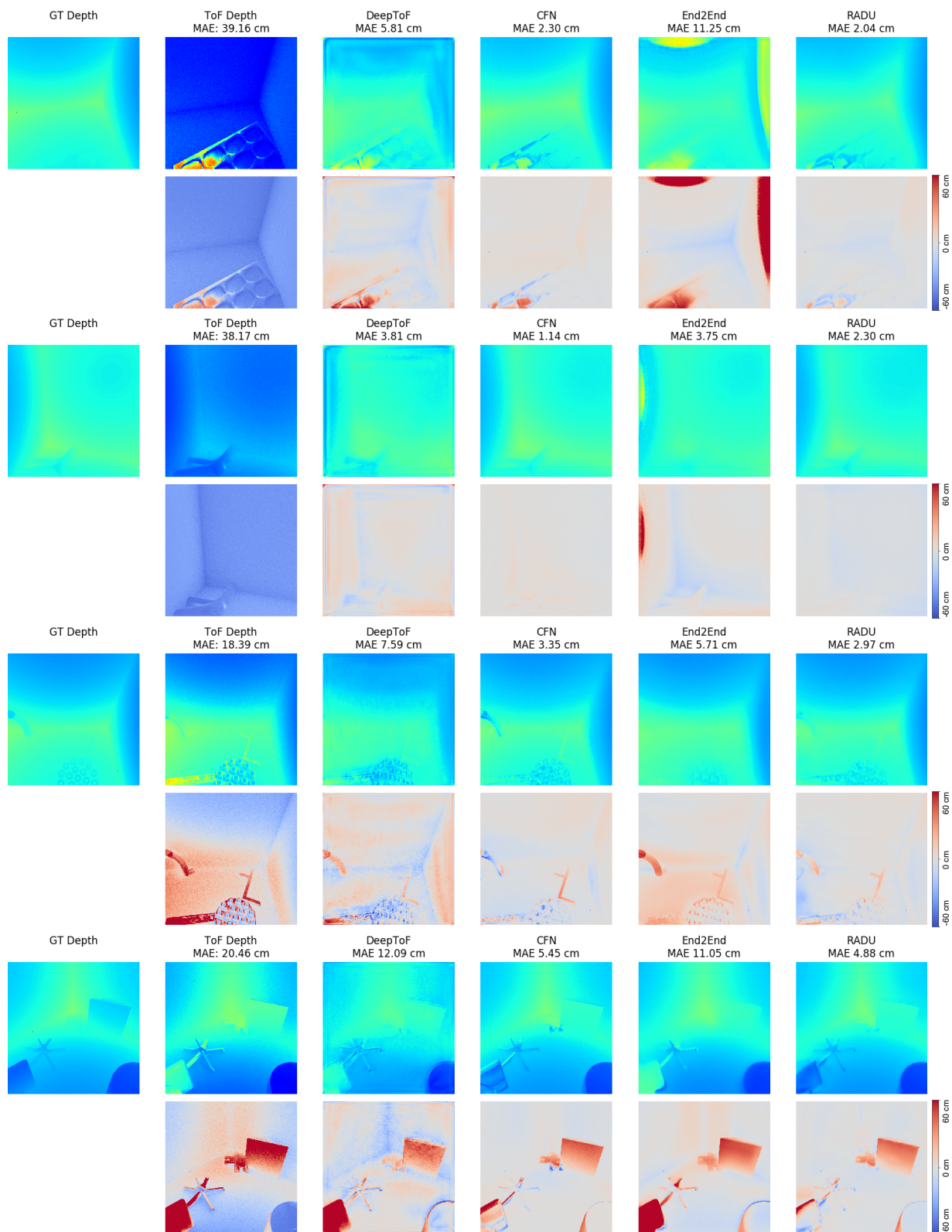


Figure 16. Results on the Cornell-Box Dataset. First rows show depths, second rows show error maps.

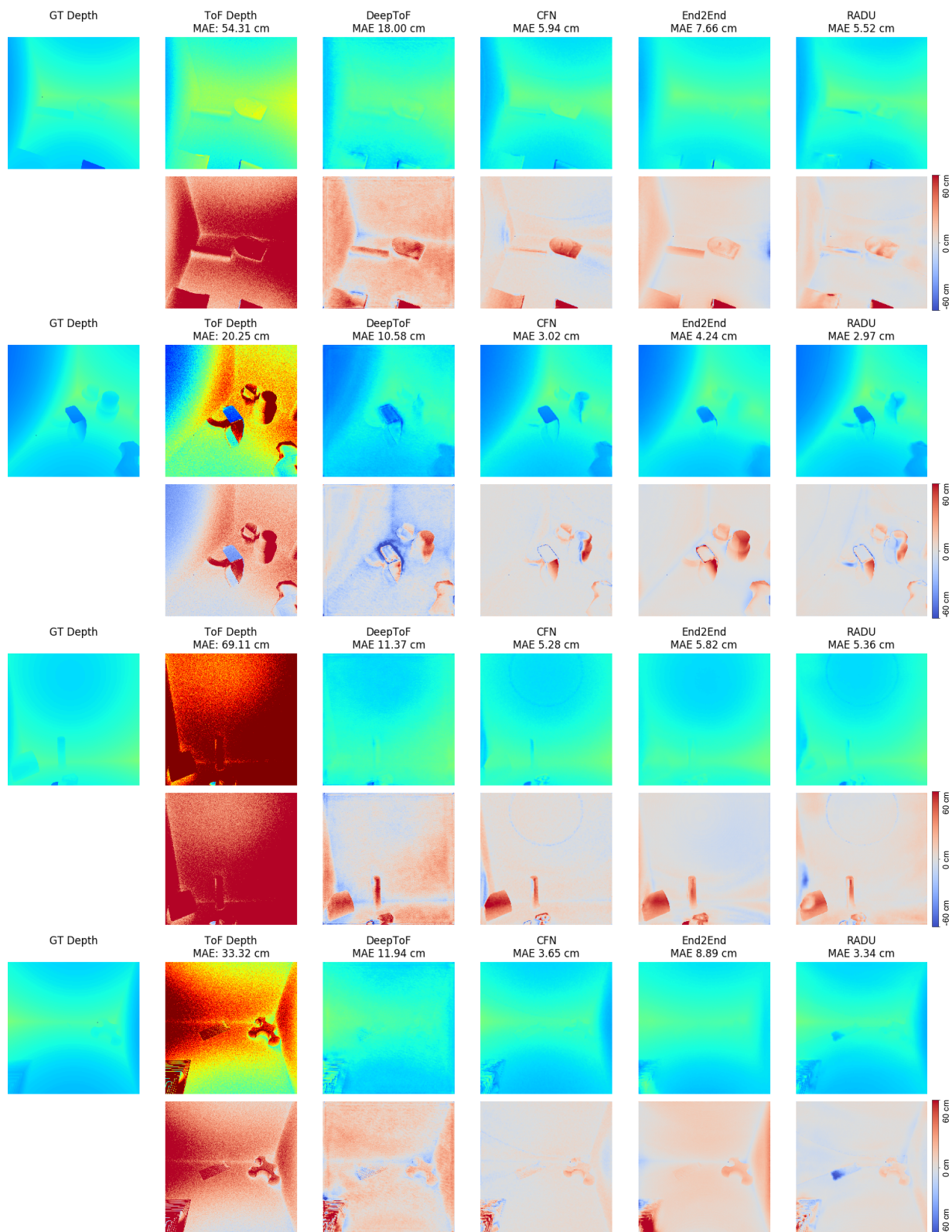


Figure 17. Results on the Cornell-Box Dataset. First rows show depths, second rows show error maps.

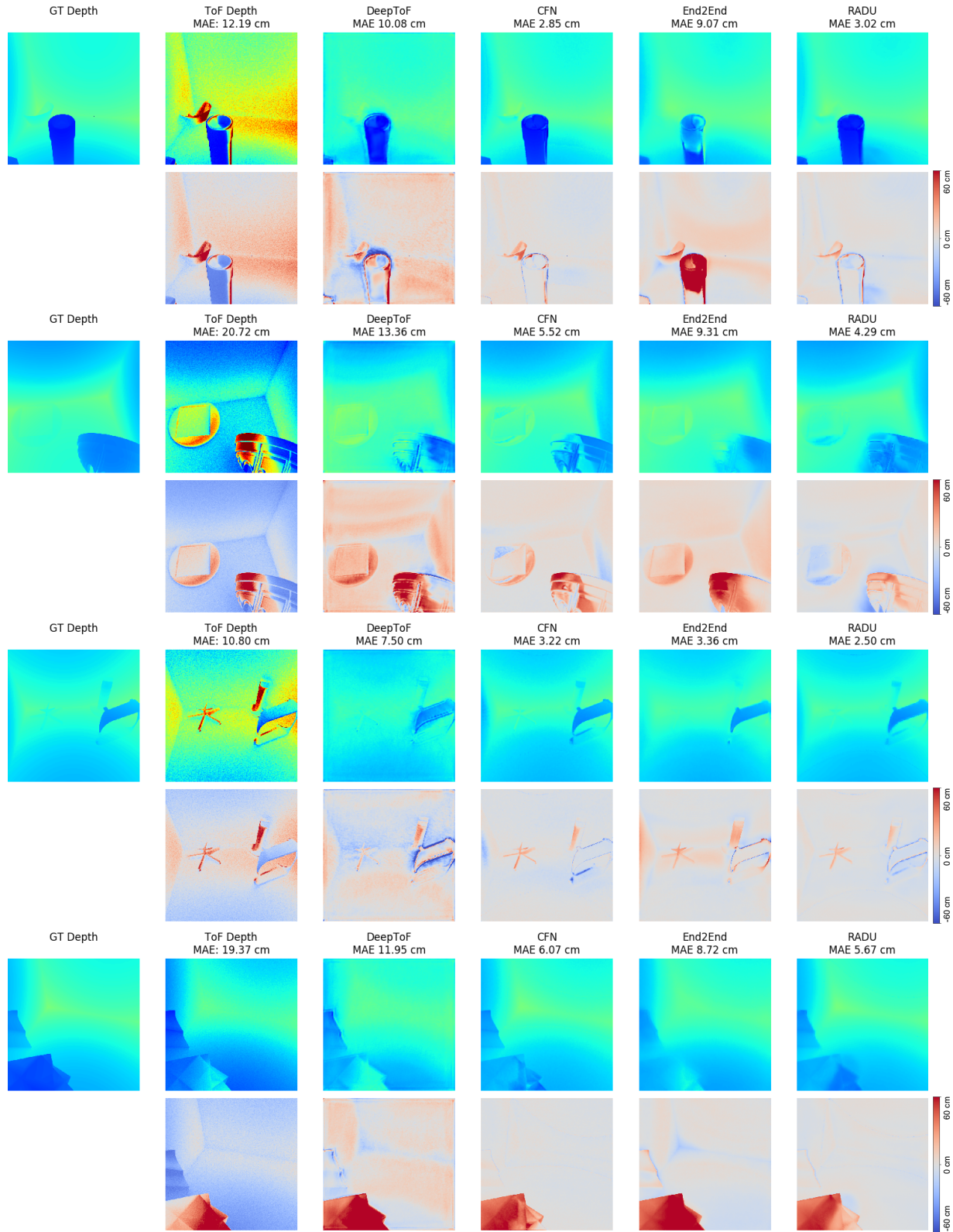


Figure 18. Results on the Cornell-Box Dataset. First rows show depths, second rows show error maps.

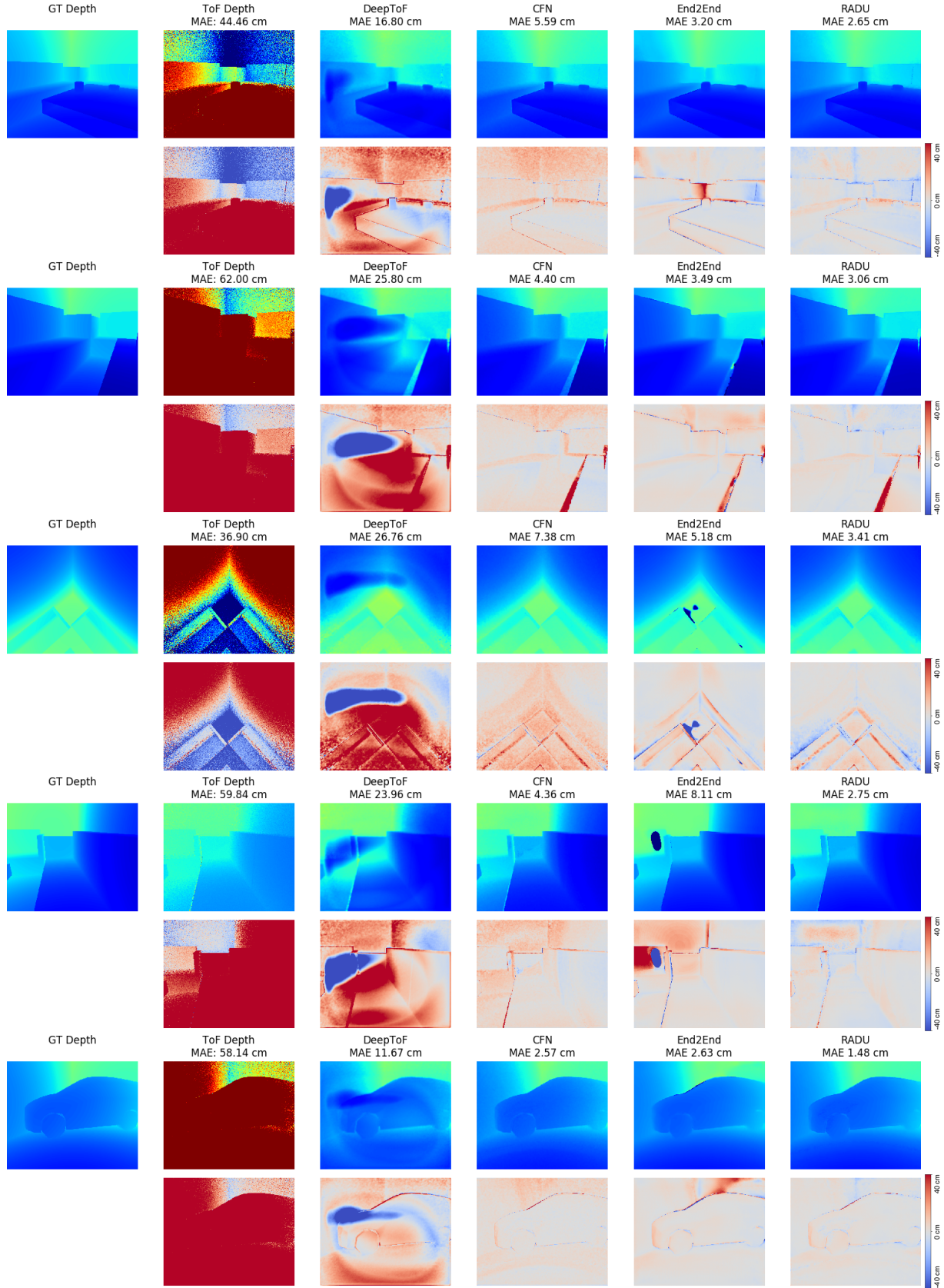


Figure 19. Results on the FLAT Dataset. First rows show depths, second rows show error maps.

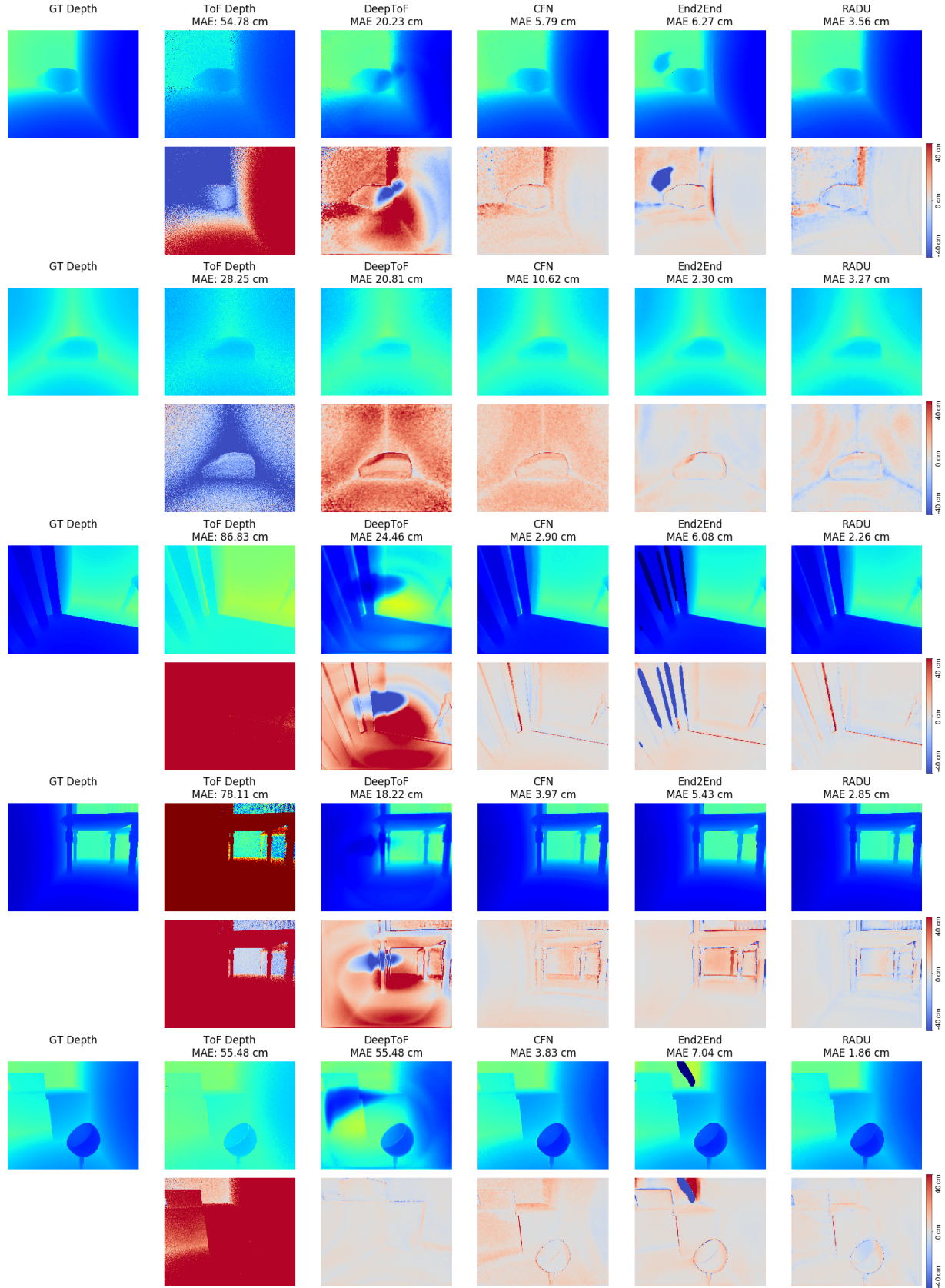


Figure 20. Results on the FLAT Dataset. First rows show depths, second rows show error maps.

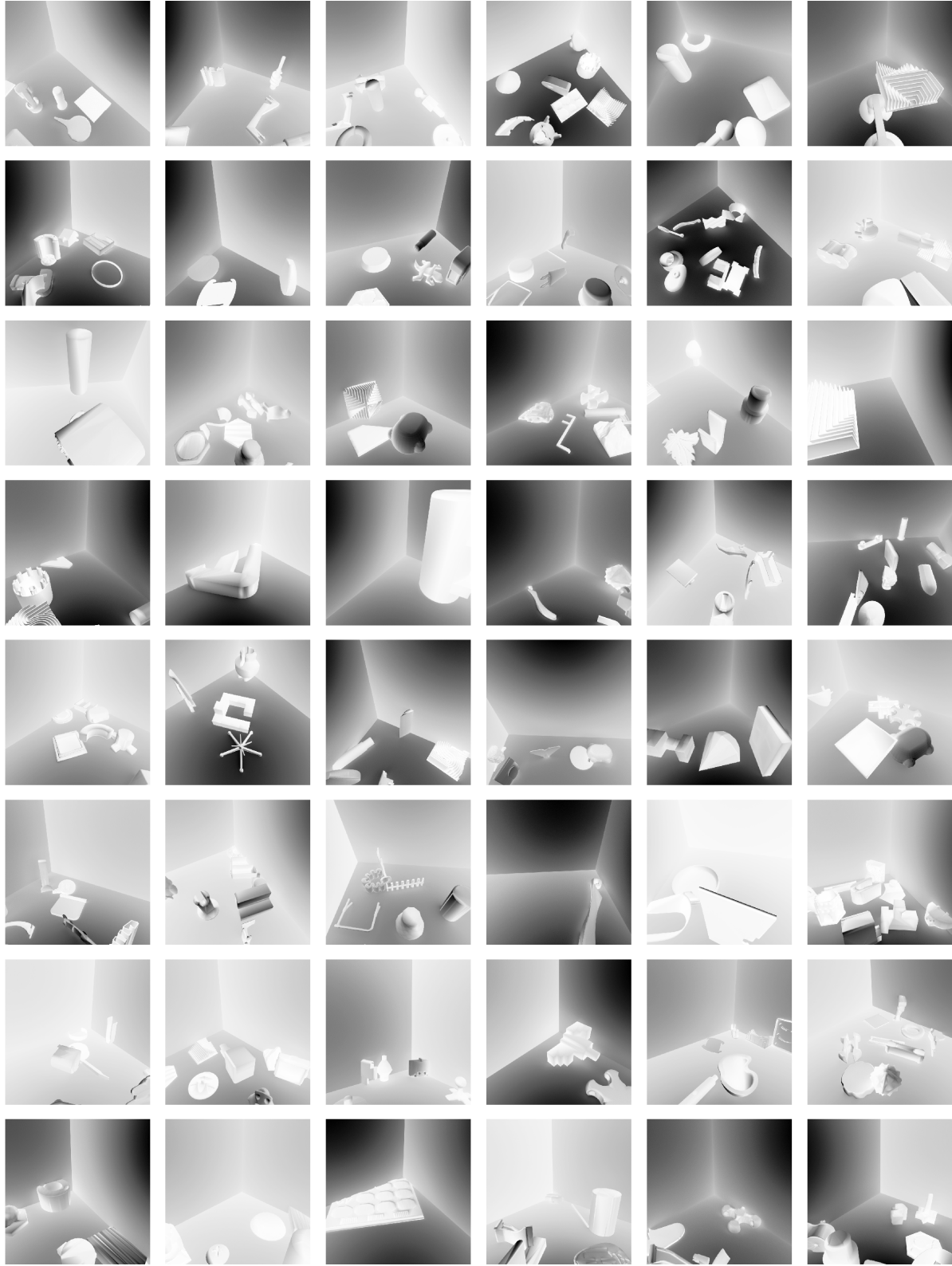


Figure 21. Example images showing one of the 50 view points with one of the three material configurations for each of the scenes in our Cornell-Box dataset. We show the intensity I at a frequency of 20 MHz as given by Eq. (18).

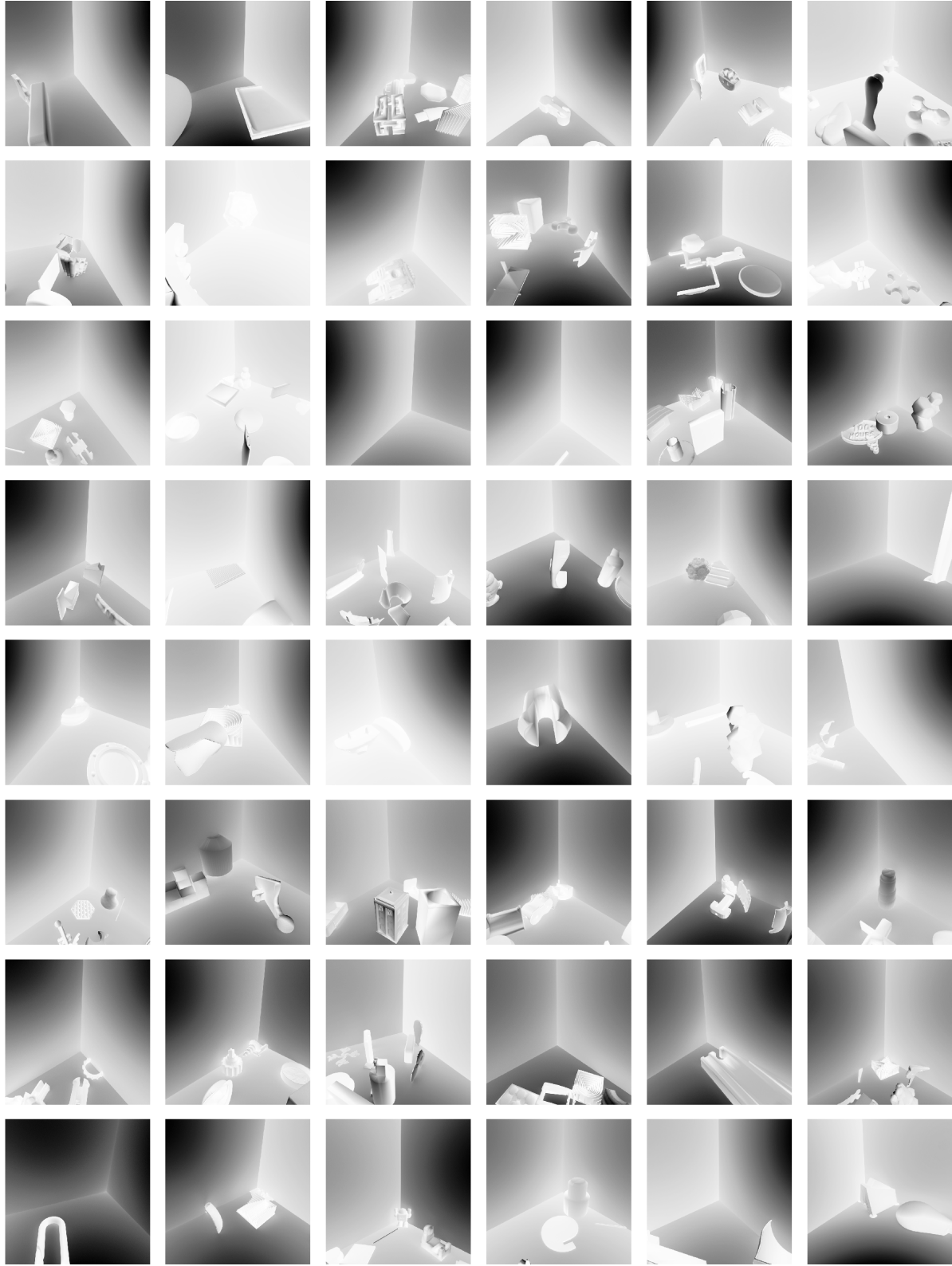


Figure 22. Example images showing one of the 50 view points with one of the three material configurations for each of the scenes in our Cornell-Box dataset. We show the intensity I at a frequency of 20 MHz as given by Eq. (18).

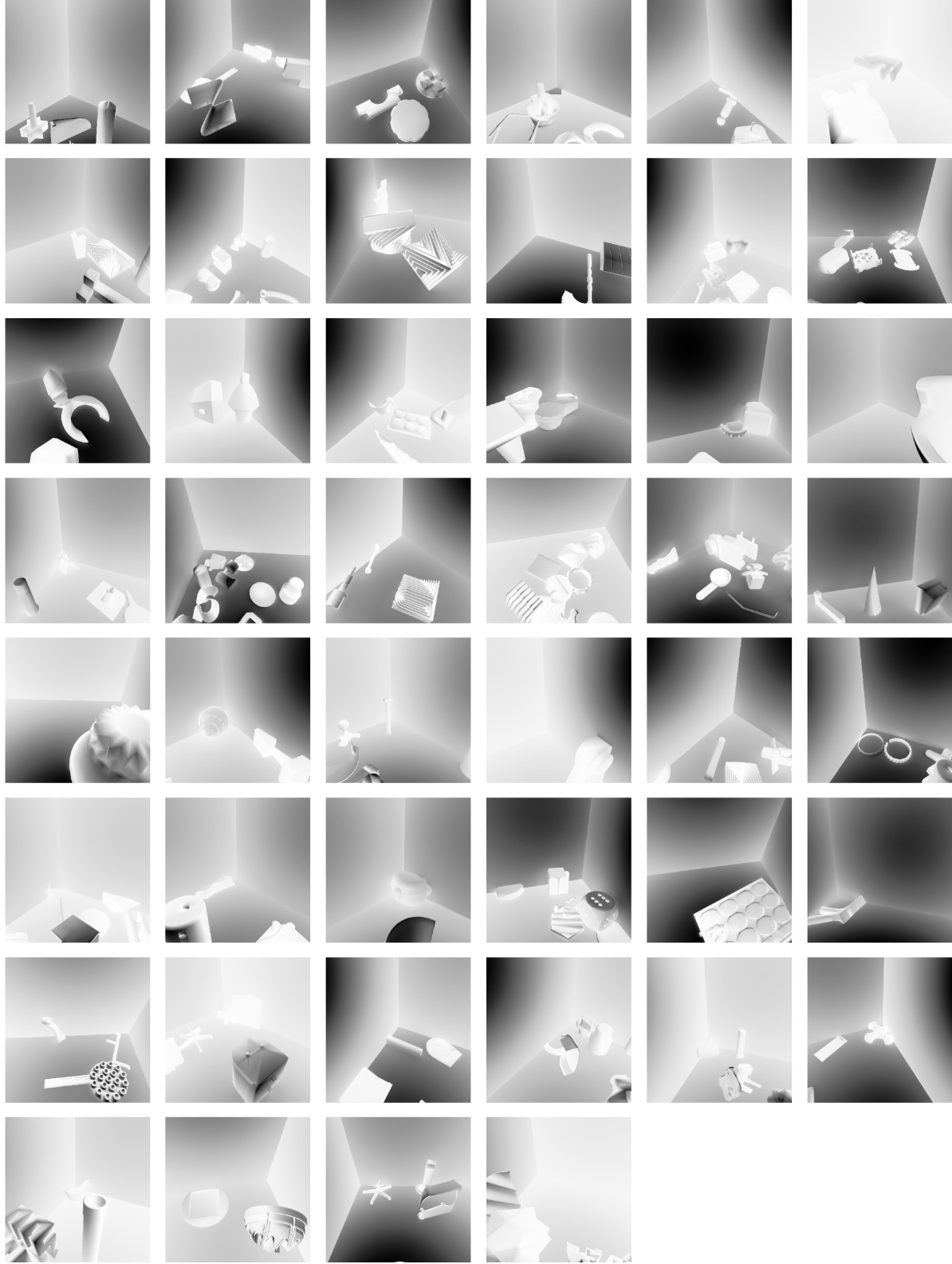


Figure 23. Example images showing one of the 50 view points with one of the three material configurations for each of the scenes in our Cornell-Box dataset. We show the intensity I at a frequency of 20 MHz as given by Eq. (18).